General Disclaimer

One or more of the Following Statements may affect this Document

- This document has been reproduced from the best copy furnished by the organizational source. It is being released in the interest of making available as much information as possible.

- This document may contain data, which exceeds the sheet parameters. It was furnished in this condition by the organizational source and is the best copy available.

- This document may contain tone-on-tone or color graphs, charts and/or pictures, which have been reproduced in black and white.

- This document is paginated as submitted by the original source.

- Portions of this document are not fully legible due to the historical nature of some of the material. However, it is the best reproduction available from the original submission.

NASA CR-175313

PRINCETON UNIVERSITY OBSERVATORY
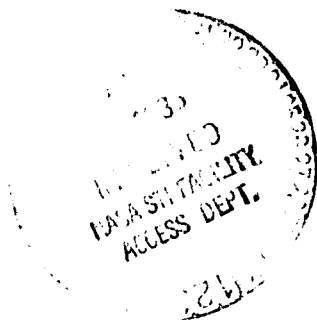Princeton, New Jersey 08544

FINAL PROJECT REPORT

for NASA Contract
NAS5-26268

Interstellar Medium Absorption Profile Spectrograph (IMAPS)

Covering the Period
August 21, 1980 to June 30, 1985

Submitted to:

GODDARD SPACE FLIGHT CENTER
NATIONAL AERONAUTICS AND SPACE ADMINISTRATION
Greenbelt, MD 20771

By: *Edward B. Jenkins*

Edward B. Jenkins
Principal Investigator
Princeton University Observatory
Princeton, N. J. 08544
Tel: 609-452-3826

August 27, 1985

TABLE OF CONTENTS

1. BACKGROUND

In 1978 NASA released an announcement of opportunity (AO) which requested research groups to submit proposals for experiments to be flown on future Spacelab missions. In response to that AO, Princeton University and the Ball Aerospace Systems Division (BASD at Boulder, Colorado) teamed up[1] to submit a proposal in November of that year to fly a high-resolution spectrograph for observing hot stars in the ultraviolet.

The payload instrument, called the Interstellar Medium Absorption Profile Spectrograph (IMAPS), was an ultraviolet echelle spectrograph which could record stellar spectra from 965 to 1165Å with a wavelength resolving power $\lambda/\Delta\lambda = 2\times10^5$ (i.e., < 0.01Å).[2]

There was a two-fold motivation for building and flying IMAPS, one scientific and the other technical. The scientific purpose, outlined in detail in §§ 4 and 5, was to establish an observing program with an instrument which could reach beyond the capabilities of the telescope-spectrometer built by Princeton for the *Copernicus* satellite. This new initiative was to build upon the earlier pioneering conclusions on the nature of the diffuse interstellar medium which were derived from the many years of operation of *Copernicus*. Specifically, we felt a strong need for having an instrument which could record stellar spectra in the astrophysically important wavelength range extending from the Lyman limit (912Å) to the vicinity of 1100 to 1200Å, but with significantly higher wavelength resolving power than that provided by *Copernicus* ($\lambda/\Delta\lambda = 20,000$).

[1]The initial decision to respond to the NASA AO was made by the scientific investigation team at Princeton. Far in advance of writing the proposal, Princeton decided that it would be beneficial to enlist the help of an aerospace instrument development contractor to create the initial instrument concept and prepare the proposal. Appendix A of this report gives a detailed account of how we competitively solicited a potential partner and how BASD was selected.

[2]This description applies to IMAPS in its present form. The original proposal called for a broader wavelength coverage (925-1315Å) and a lower resolution (1.3×10^6).

The main technical objective was to have a program which made use of a new photon-counting ultraviolet detector developed   rinceton. The initial exploration on the feasibility and operating characteristics of the device was supported by a NASA SR&T grant to Princeton (NSG-7618). This detector, a windowless, Intensified CCD camera (ICCD) described in §6.4, represented a very promising candidate concept for a two-dimensional image sensor to be used on future space astronomy enterprises which must function at wavelengths covered by IMAPS (such as the proposed *Lyman* [*FUSE*] Explorer mission).[3] By 1978, we had reached a point in the detector program where flight instrument development was an ideal way to bring forth a more mature design. Also, we knew that ultimately we would need to prove that the detector could function well in an actual flight environment before it would be an acceptable candidate for ultraviolet instrumentation in general.

On the basis of a Category III rating by the peer review of our proposal, NASA turned down our request for a Spacelab mission assignment. While the proposal was judged to have excellent scientific merit, some apprehension was expressed about the technical risk in trying to fly a detector which was not proven. On the basis of this evaluation, we felt it was proper to resubmit our proposal within the framework of a sounding rocket research program. The appropriateness of this strategy was underscored by the basic philosophy of the NASA sounding rocket research effort, namely, to allow investigators to develop new instrument concepts at low cost, with a generous flexibility in schedule, and without the risk that

---

[3] Many other detector configurations suitable for far-uv wavelengths use a microchannel plate with a photocathode deposited on the front surface. Photocathodes operating on the rugged terrain of an MCP have two drawbacks, of as yet undetermined severity, when compared with monolithic photocathodes on a solid substrate employed by the Princeton ICCD. The discontinuous structure and complicated E fields of the MCP photocathodes result in 1) a lower overall quantum efficiency and 2) spatially periodic modulations in response caused by the MCP pore structures which can produce undesirable effects if the images have small-scale details. The latter effect has yet to be measured directly, but its existence seems very plausible.

technical difficulties or initial flight failures would jeopardize the large investment of a complex flight program.

The initial submission of a proposal for sounding rocket research using the IMAPS instrument was made in July 1979. This proposal was followed by amended budgets and schedules in November 1979 and March 1980. On August 21,1980, NASA awarded (through the Goddard Space Flight Center) contract NAS5-26268 to Princeton University to embark upon the proposed program. In line with our original commitment to BASD in our proposal writing agreement, we engaged them under subcontract to build the payload and support testing and flight operations. The effort we outlined called for building IMAPS to fly on Black Brant rockets, with the ultimate intent of converting it to operate on Spartan missions in accord with the NASA's planned transition from suborbital to orbital transportation of small astronomical payloads.

2. HISTORICAL SUMMARY OF THE PROGRAM

The design, procurement of parts and assembly operations at BASD advanced in an orderly fashion from late 1980 to mid-1982. To a good approximation, we were able to maintain the program within the projected costs and schedule throughout these phases. After the basic payload fabrication had been completed in late 1982, NASA support was shifted from the contract discussed in this report to a grant (NAG5-616) since the remaining effort was to be primarily mission operations, payload refurbishment and scientific research, rather than the initial procurement of a complicated instrument from a subcontractor.

In preparing the payload for flight, we experienced a delay of about one year after we discovered the sensitivity of IMAPS was at least one or two orders of magnitude too low. Ultimately, we traced the difficulty to problems with the imaging detector (see §7.1). Specifically, the design of the on-chip amplifier for the CCD

that we purchased initially was not good enough to give us the necessary charge sensitivity and high-frequency response to detect individual photoelectrons. Also, its charge transfer efficiency was not adequate. In early 1984 we obtained from RCA a CCD with a newer design. This CCD showed excellent operating characteristics, and as a result, the earlier difficulties with our detector were surmounted very effectively.

The first launch of the IMAPS instrument on a Black Brant rocket occurred on October 5, 1984. Unfortunately, on this flight there was a catastrophic inrush of air into the payload. The severely degraded vacuum caused the detector's high voltage system to break down and as a result we were unable to obtain any data. An analysis of the probable cause of this failure is discussed in detail in §7.2.

Shortly after the first flight of IMAPS, BASD began refurbishment of the payload for a second flight. Concurrently, we started an investigation on what caused the vacuum failure and what steps we would take to minimize the chances that it could occur again. After we had satisfied ourselves that we had worked on the vacuum problem as thoroughly as possible, we embarked on final preparations for the second flight.

The second flight of IMAPS occurred on April 20, 1985. All of the payload systems functioned perfectly, and excellent recordings of the data were obtained. We were not only pleased with the quality and quantity of scientific information available from this flight, but also we gathered valuable indications on how well the ICCD image sensor can perform in a space environment. A discussion of the preliminary conclusions from the flight data is contained in §7.3.

In response to a solicitation from NASA Headquarters to existing sounding rocket experimenters, we submitted a proposal in June 1984 to convert IMAPS for operation on Spartan and fly it in early 1988. In early 1985 we learned that NASA accepted our proposal. Currently, the payload is being reconfigured so that it will

operate on Spartan.

3. INSTRUMENT OVERVIEW

The payload we flew on sounding rockets and Spartan was a slitless, objective grating spectrograph which recorded ultraviolet stellar spectra at a resolution of approximately 0.004Å (profile FWHM) and with a sample interval (pixel width) of 0.002Å over the very difficult wavelength range 965 < λ < 1165Å , a region of extreme scientific importance. A key feature of the optical design was its extreme simplicity; aside from a mechanical collimator which restricts the field of view to a one degree circle to eliminate confusion from nearby stars, the incident starlight interacts with only two optical elements before it is imaged. First, the parallel beam hits an echelle grating. Diffracted light from the echelle then goes to a parabolic cross-disperser grating which images the spectrum on a 1.5 cm diameter photocathode in a windowless, photon-counting Intensified CCD detector (ICCD). The system is illustrated in Figure 1.
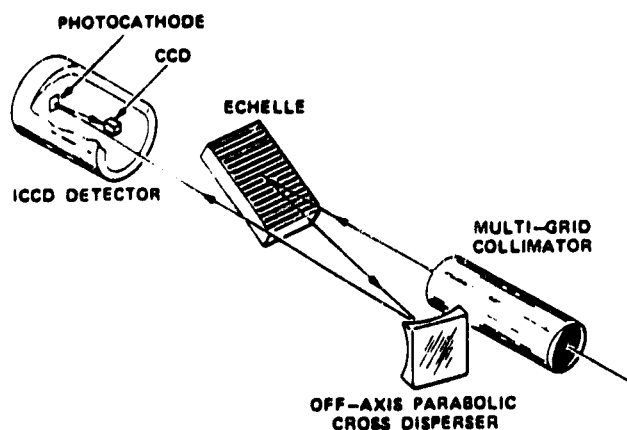

Figure 1

The high wavelength dispersion of this instrument was achieved by having the

echelle set at a large angle of incidence (63°) and employing a very long focal length for the cross-disperser (1800 mm). While the area of the entrance aperture was only 250 cm^2, the light collecting power of the instrument was very good for a device working in this wavelength interval because there were relatively few reflections and the KBr photocathode, being opaque and on a solid substrate, had a high quantum efficiency. This payload was built to fit within the standard Black Brant sounding rocket envelope (17-inch diameter cylinder).

The principal research motive was to build upon the pioneering investigations from the uv spectrometer and telescope on the *Copernicus* satellite, but with a quantum leap forward in wavelength resolving power (a factor of 10). As implied by the name of our instrument, *Interstellar Medium Absorption Profile Spectrograph* (IMAPS), the greatest emphasis was to obtain very accurate line profiles from absorption features which are produced by constituents in the interstellar medium, both atomic and molecular.

There are, of course, other areas of astrophysical research which also will benefit enormously from observations by IMAPS. Much can be learned about the composition, dynamics and overall structure of hot stellar atmospheres, and likewise for the chromospheres around relatively cool stars. If special instrumental accommodations are made, IMAPS can even make unique observations of solar system objects, since its large dispersive power would, in all likelihood, enable us to record simultaneously the images of various emission features without overlap. Nevertheless, while these other research areas are important, the main emphasis of the research supported by this contract centered on contributions IMAPS could make in furthering our knowledge of interstellar matter, since this is where the particular strengths of IMAPS gave the greatest additional leverage. Also, this topic was the chief area of interest to the Principal Investigator.

Over the quarter-century span of NASA's existence, we have witnessed an impressive growth in the power of uv space astronomy instruments to gather information. In certain respects, IMAPS represents a continuation of this trend, even within the shadow of far larger and more costly ventures which operate at longer (and easier) wavelengths. The diagram in Figure 2 illustrates this point.

Figure 2
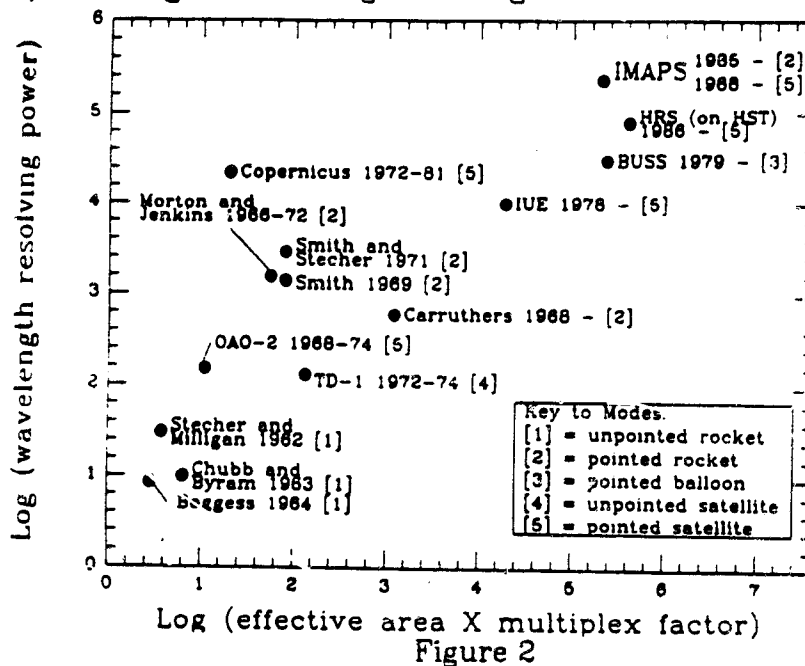
On logarithmic scales we see a comparison of two important attributes for some selected past and present astronomical missions (and one future one). A very fundamental measure of a uv instrument's usefulness is its wavelength resolving power, expressed here in dimensionless form $\lambda/\Delta\lambda$. The logarithm of this quantity is represented by the y axis. On the x axis is plotted the logarithm of each instrument's *effective aperture area*, in cm^2 (i.e. the product of collecting area, instrument efficiency and detective quantum efficiency[4]), multiplied by the instrument's capability of multiplexing (i.e., simultaneously recording) many different wavelength elements. The latter quantity measures how rapidly one can record all of the elements of a spectrum to a given level of accuracy for a star of a

_____

[4]Instruments using photographic emulsions directly were assumed to have a DQE = 3%.

particular brightness. (Of course, if one's objective is to study only one or two specific lines in a spectrum, large multiplexing powers offer no real advantage.) The location of the point for IMAPS in this diagram reveals the forward-looking character of this mission, within the framework of NASA's overall program in uv space astronomy.

4. GENERAL SCIENTIFIC RATIONALE

4.1. Wavelength Coverage

For astrophysical spectroscopy, wavelengths extending from approximately 1150Å down to the Lyman limit at 912Å are of particular interest and present a special challenge to astronomers. Observations at these wavelengths must occur from space vehicles and must be performed by instruments which contain no transmission optical elements nor detectors which have front windows. In designing and building the telescope and spectrometer aboard the *Copernicus* satellite, extra effort was spent to incorporate all-reflective, LiF-overcoated optics and open-face photomultipliers so that the spectral coverage could extend below 1150Å . With *Copernicus* out of operation, IMAPS now provides the only opportunity to observe spectra at high resolution from celestial sources at these wavelengths. The spectrographs aboard *IUE* and those proposed for the *Hubble Space Telescope* incorporate detectors with MgF_2 or LiF faceplates to support a photocathode, and these instruments have virtually no sensitivity at the shorter wavelengths.

A topic which merits some discussion is the scientific reason for placing a special emphasis on the wavelength range covered by IMAPS, which is situated within a very much larger span of the spectrum to be studied from space vehicles. We believe these shortest wavelengths have a unique importance, and to understand why, we may look back upon some of the research achievements of the *Copernicus*

satellite. Over its eight years of operation, this instrument has allowed us to exploit the ultraviolet spectra of hot stars for their plentiful and scientifically lucrative absorption features.

For the interstellar medium, *Copernicus* has allowed us to obtain for the first time an extensive overview of the patterns of element abundances, measure the distribution and rotational excitation of molecular hydrogen, witness tremendous contrasts in temperature and ionization, and register the widespread presence of rapidly moving parcels of gas which have been influenced by energetic phenomena. Many of the most interesting conclusions were derived from lines which *only* appear below 1165Å :

[1] All of the electronic transitions from the ground vibrational state of H_2 occur below about 1140Å . For one star (ζ Pup), the equivalent widths of well over a hundred lines from different rotational levels were measured.

[2] The amount of deuterium produced in the early development of the universe is best indicated by interstellar *atomic* abundances of D because deuterated molecules are modified by chemical fractionation. High order members of the Lyman series must be observed since the Lα (and frequently Lβ) lines from interstellar hydrogen are broad enough to swamp the accompanying deuterium lines.

[3] Principal lines of the Lyman system of HD start at 1106Å and go shortward. When compared with the abundance of H_2 and evaluations of the interstellar ratio of atomic D and H, measurements of HD inform us about the rates of ion-molecule reactions in clouds, which in turn are governed by the rates of hydrogen ionization by low-energy cosmic rays and x-rays.

[4] The widespread presence of a very hot phase (T >> 10^5K) of the interstellar medium was signaled by absorptions from O VI at 1032 and 1038Å . Other highly ionized atoms which have absorptions at longer wavelengths, such as N

V, C IV, and Si IV, are hard to interpret because they can be produced either by collisional ionization in a hot gas or photoionization from very hot stars. O VI is by far the most conspicuous tracer of coronal gas in our galaxy because its cosmic abundance is fairly high, and its peak fractional abundance from collisional equilibrium occurs at the prevailing high temperatures.

[5] There are other astrophysically important atoms or ions with transitions from the ground state producing absorption features *only* below 1150Å ; to name a few, there are C III (977Å), N II (1084Å), N III (989Å , often difficult to separate from a nearby feature of Si II with the resolution of *Copernicus*), F I (952, 955Å), P IV (951Å), S IV (1063Å), S VI (933, 944Å), Cl II (1064, 1071Å), Cl III (1005, 1009, 1015 Å), Cl IV (973Å), A I (1048, 1066Å), and Fe III (1122Å , often there's interference from nearby C I lines).

Frequency Distribution for Interstellar
Absorption Lines vs Wavelength
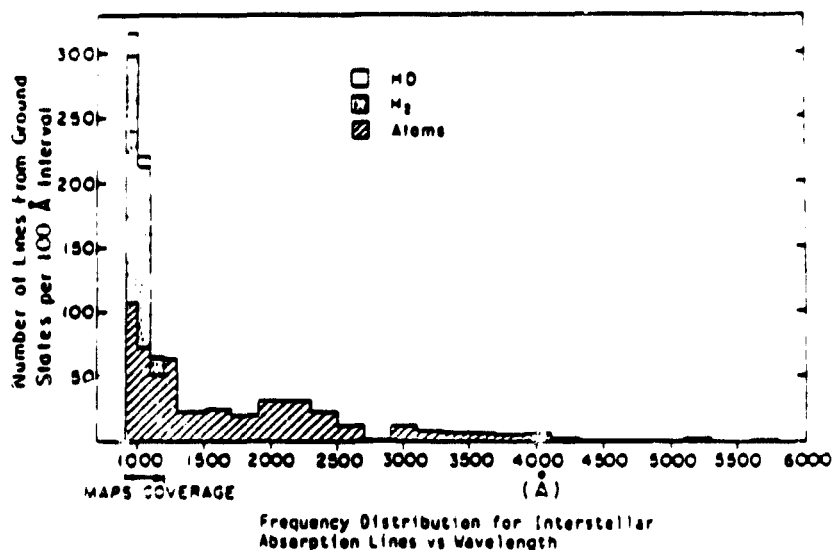
Figure 3

An alternate, though simplistic, approach to grasping the relative importance of certain wavelengths is merely to count the number of likely interstellar absorption lines which could appear in a given spectrum.[5] Figure (3) shows the

[5]Atomic lines and their approximate f-values were taken from a comprehensive compilation by Kurucz and Peytremann (SAO Special Report 362). For a line to be counted, it had to be strong enough to give a 6σ detection for a 500 s exposure of a 5th magnitude BO star with a color excess E(B-V) = 0.10. A column density of 5×10^{20} cm^{-2} times an element's solar abundance relative to H

distribution of such lines with wavelength. For the atomic lines, only those from the ground state were included; many atoms will show additional absorptions from collisionally excited fine-structure levels. The large number of H_2 lines gives an impressive advantage to the score for $\lambda < 1100\text{Å}$, but even if we discount this fact we find the density of atomic lines surpasses that of the longer wavelengths.

4.2. Wavelength Resolving Power

A substantial increase in spectral resolving power is by far the most important contribution that IMAPS will offer for progress in research on interstellar matter. As illustrated in Figure (2), the anticipated velocity resolution of 1.3 km s^{-1} for IMAPS will surpass that of all past missions, as well as those currently planned, to record uv stellar spectra.

There are a number of important benefits which arise when spectra are recorded at increased resolution. Weak and narrow interstellar lines are more easily localized in velocity, and fewer nearby continuum photons, which add to the noise, are blended into the profile (for perfectly smooth stellar continua at a given intensity, the sensitivity to weak lines is inversely proportional to the square root of the velocity interval over which the line must be measured). Also, the better resolution permits us to distinguish narrow interstellar lines with greater ease when stellar features are not greatly broadened by rotation.

A fundamental problem with spectra of only modest resolution is that, in most instances, equivalent widths and average velocities are the only attributes of the lines which can be measured with much reliability. As a consequence, when lines

was assumed. The strengths of H_2 transitions were computed for a combination of two populations, one with $N_{J=0} = 3\times10^{13}\text{cm}^{-2}$ and $T_{rot} = 1000$ K and the other with $N_{J=0} = 10^{19}\text{cm}^{-2}$ and $T_{rot} = 100$ K. There was no verification that lines did not interfere with each other by chance, so possibly in a few crowded areas the actual numbers of useful lines will be slightly less than those shown.

become saturated one must resort to curve-of-growth techniques to obtain column densities. Uncertainties in the real behavior of these curves was the most important factor which limited the precision in interpreting *Copernicus* data, at times giving at least an order of magnitude uncertainty in abundances.

When the resolving power is high enough to show the exact *shape* of a profile, one may derive optical depths $\tau(v) = -\ln[I/I_{continuum}]$ at every point and integrate them over over all velocities to obtain an unambiguous answer for the column density, using a single absorption line with no reliance on a curve of growth whatsoever. The only requirements for the success of this method are that *a)* the zero intensity level is known accurately, *b)* the finest detail in the velocity structure is not much smaller than the resolution, and *c)* the profile is not too strongly saturated (for instance, central transmission $\gtrsim$ 5% or maximum $\tau \lesssim$ 3).

From the above arguments, we see that improvements in resolution are beneficial for the study of both weak and strong lines. In effect, both ends of the dynamic range are extended for detecting and interpreting lines of differing strength. This leads to a substantial improvement in the availability and usefulness of absorptions from both common and rather scarce atoms, ions and molecules. Beyond this, however, there also should be a many-fold increase in our chances of untangling the superposition of lines from different regions along a line of sight if we have the velocity resolution to identify components which are slightly displaced from each other. To fully grasp how frequently complicated arrays of narrow components are seen bunched together over narrow velocity ranges, we need only to look at scans of interstellar absorption lines recorded at visible wavelengths with a resolution of $\sim$ 1 km s^{-1}, such as those published over many years by L. Hobbs and his associates. Finally, as the following section outlines, the increased resolution is valuable for solving some specific scientific problems in interstellar matter research.

5. SPECIFIC RESEARCH GOALS

5.1. Physical State of H I Regions

OBJECTIVE: to unravel the widely varying regimes of pressure, temperature, radiation density, composition and chemistry within neutral clouds.

Most of the gas in our galaxy resides within regions which predominately contain neutral atoms. Recently, we have become more keenly aware of the heterogeneity of these H I regions, which are characterized by substantial differences in temperature, density, rates of molecular synthesis and reactions, element abundances and starlight radiation densities. However, the stratification of these attributes within individual clouds and their general statistical properties are not well known, primarily because we have been hampered by either inadequate velocity resolution (spectra recorded by *IUE* or *Copernicus*), uncertain or very broad coverage of space (radio studies of emission and absorption lines), or a poor selection of observable species (absorption lines in the visible). Further progress in understanding the structure of H I regions will be greatly facilitated by experimental methods which overcome these limitations.

For any specific observation, spectra recorded by IMAPS will delineate parcels of gas at well-defined radial velocities which probably reside within limited volumes of space, yet at the same time this instrument retains a great breadth in sampling constituents which respond in very different ways to the physical environment. For instance, the abundance of singly ionized carbon (C II) in any part of an H I region is approximately proportional to the local density of hydrogen n_H times the gas-phase abundance ratio of C to H. The density of neutral carbon (C I) is proportional to that of C II times the electron density divided by the density of ionizing radiation. The amount of this C I in either of the two excited fine-structure levels

is governed by local H I (and H_2) densities and the kinetic temperature. Doubly ionized carbon (C III) is not expected to be abundant inside H I regions, but it may be present near the cloud boundaries where it is sustained by ionizing radiation or shock heating. Observations of just these four forms of carbon (3 stages of ionization plus the CI excited levels) will enable us to better understand the density and temperature regimes inside the clouds. Neutrals and ions of other elements (e.g., Si, S, and Cl) can be used to check the conclusions derived from C.

In H I clouds which can be observed with IMAPS, the abundances of various simple molecules are very responsive to physical conditions. Molecular hydrogen is formed by the interaction of H atoms with grains and destroyed primarily by ultraviolet radiation. We can monitor the intensity of the dissociating radiation by examining the optically pumped populations of high-J rotational levels, determine n_H from intermediate-J ratios, and, if $n(H_2)/n_H$ is appreciable, measure the kinetic temperature by the rotation temperature between J=0 and 1. HD molecules are formed by an exchange of H_2 with deuterium ions; the concentration of ions is in turn governed by the rate of cosmic ray and x-ray ionizations. Thus, measurements of HD allow us to sample another important environmental influence in neutral clouds. Other molecules, such as CO and OH, are also believed to result from such exchange reactions. The rotational excitation of CO will indicate the temperatures and densities in the regions where such molecular activity is high (*Copernicus* was not able to resolve individual lines which contributed to the CO band rotation branches), and these results can be confirmed independently from the relative populations of rotationally excited HD.

Absorption lines of CH^+ are observed in the visible spectra of some stars. Since CH^+ is rapidly destroyed by an exchange reaction with H_2, we have evidence for dense regions which do not contain appreciable amounts of H_2, perhaps on the outer edges of the clouds or in recently shocked material. IMAPS, with its

excellent selectivity for velocities, can let us study CH^+-bearing regions with less interference from other dense portions of a cloud.

While most of the gas within H I regions is at a temperature $T \lesssim 100$ K, there is considerable evidence from 21-cm absorption and emission, as well as from *Copernicus* data, that some neutral gas is at substantially higher temperatures (1000 K $\lesssim T \lesssim 8000$ K). In many instances, the wavelength resolving power of IMAPS will be sufficient to measure the thermal broadening of interstellar lines directly, instead of relying on indirect determinations with the curves of growth. We can differentiate between turbulent and thermal broadening by studying atoms of different mass, since the square of the observed velocity broadening is equal to the sum of kT/m and the squares of the *rms* turbulent and instrumental profile widths. To give a quantitative illustration of how this may be done, we can consider gas with $T = 100$ K and $b = 1$ km s^{-1} from mechanical motions -- turbulence this small is often seen for profiles which show up in 21-cm absorption. Here, the weak lines of D I, N I and A I would have apparent full widths at half maximum (FWHM) of, respectively, 4.1, 3.6 and 3.4 pixels. Under these conditions the temperature broadening is just discernible. On the other hand, when T reaches 1000 K the widths increase to 8.4, 5.3 and 4.2 pixels, and the differentiation with mass is easily measurable. If weak members of the Lyman series of H I can be measured, the contrast is even greater (FWHM = 11.4 pixels at 1000 K with $b = 1$ km s^{-1}). If b were as large as 10 km s^{-1} in the warm H I regions, emperatures on the order of 1000 K would still render D I lines which are wider than those of the heavier lines by 1 pixel.

The origin and distribution of the *warm* H I gas are poorly known. Is there a continuous distribution of material which pervades most of the space between the cool clouds? Are there discrete packets of warm gas, as with cooler material? Or, as a third alternative, is most of the warm H I situated in a transition zone where

partial ionization is occurring between a cool cloud surface and a much hotter (and fully ionized) environment? We can obtain a great deal of insight on these possibilities, inasmuch as observations with IMAPS will enable us to identify isolated velocity components of H I at appreciable temperatures, assess their number per unit volume of space, and recognize any correlations of their velocities with those of the cooler clouds. The association of hot and cool H I gas may explain the apparent intermediate temperatures (where thermal instabilities should occur) deduced from comparisons of 21-cm absorption and emission.

5.2. Investigations of H II Gas

OBJECTIVE: to isolate absorption lines from fully ionized regions and use them to reveal the pervasiveness and character of ionizing processes.

By observing ions which could not be produced by photoionizations less energetic than those which ionize hydrogen, we can identify absorption components which arise from gases which are almost fully ionized. The most useful of these lines are those which are weak; a great preponderance of such features occur at the very short wavelengths covered by IMAPS. The velocities of these profiles permit us to identify which components of neutral or weakly ionized atoms arise from H I regions and which come from H II regions. Only on rare occasions when the velocity separations were particularly favorable was this done successfully with the *Copernicus* observations. IMAPS should have sufficient resolution to make such detailed component identifications commonplace.

Interesting conclusions about the topological relationships of H I and H II regions should arise from global comparisons of their respective velocity components. If H II regions are isolated domains restricted to the neighborhoods of hot stars, we would expect to find an H I component associated with each H II

component, but with a vast number of H I clouds which are not accompanied by ionized gas. On the other hand, if the neutral gases are strongly clumped, the H I clouds will be embedded in a low density medium which can be ionized by stars, since the Lyman-limit photons (and soft x-ray background) will have a long mean free path. Then, nearly all of the H I clouds would be bathed in ionizing radiation and moderately dense H II zones would surround them (and share their velocity).

As with H I regions, temperatures and velocity dispersions can be measured independently from the line widths of individual H II components. Ions in excited fine-structure levels preferentially reside within the denser clumps of gas, which allows us to determine how frequently such condensations occur and how their temperatures differ from the low density material. The radiation fields from stars which are isolated from others[6] can be determined by studying the ionization ratios Fe II/Fe III, P II/P III and S II/S III, since their lines are weak and unsaturated. On some occasions ratios of stronger lines will yield reliable ratios, e.g., Si II/Si III, C II/C III and N II/N III. Also, we shall be able to measure the relative depletion of elements of H II regions and compare them with the patterns from element to element (i.e., refractories vs. volatiles) found in H I regions. Of the doubly ionized species just discussed, the HRS coverage does include S III, P III and Si III. However, the latter is frequently strongly saturated, or inside the core of a strong stellar Si III feature, and the former two can be blended with nearby strong interstellar resonance lines. Finally, we can draw together our results on heat inputs (from stellar radiation fields)and cooling rates (which are governed by the abundances and densities), and derive self-consistent models to explain the observed temperatures.

---

[6]A survey by IMAPS will tend to emphasize such stars, since neighboring stars of comparable magnitude must be more than $1°$ away.

5.3. Coronal Gas and Transition Regions

OBJECTIVE: to test a number of theoretical alternatives on the origin of gases with $T \sim 10^5$ - 10^6 K by mapping the detailed structure of O VI absorption profiles.

A major surprise from the initial surveys of stellar spectra by *Copernicus* was the discovery of ubiquitous O VI absorption features (at 1032 and 1038Å), which indicated the widespread presence of coronal gas in space, with $T \sim 4 \times 10^5 K$. Observations of diffuse, soft x-ray emission indicate the existence of material at even higher temperatures $(T > 10^6 K)$. While the *Copernicus* and x-ray emission data have yielded extensive information on the general properties of the coronal gas, such as average density, temperature, regional distribution, and so forth, an important attribute which has eluded us is the fine-scale distribution of this gas. For instance, is O VI evenly distributed over extensive voids between cooler concentrations of material, or do the observed profiles arise from confined regions, perhaps many in number, which move about at random and create composite profiles over the many hundreds of pc of typical lines of sight? We are still uncertain even about what fraction of all space is filled with coronal gas.

As with the early studies of cool matter from the visible absorption and radio emission lines, the key to understanding the morphology and origins of O VI regions is founded upon detailed studies of velocity structures. IMAPS will, for the first time, permit such investigations to be performed without having to correct for instrumental smoothing. We will search for O VI components which seem to be correlated with ordinary H I (or H II) velocity peaks. Tentative indications that these very different phases have a kinematical link have been derived from data recorded by *Copernicus*. Persuasive theoretical arguments indicate that O VI lines may arise from evaporative interfaces between the envelopes of cool clouds and a

much hotter medium. By carefully measuring the velocity displacements and column densities of these correlated O VI peaks (if they exist), we can compare our results with theoretical models for velocity gradients across evaporative flows, and in turn use this information to derive the overall energy and mass exchange budgets between the cool clouds and the surrounding very hot medium. The total energy flow can, in turn, be checked for consistency with our estimates of overall energy inputs from supernovae and O-B associations to ascertain the importance of this phenomenon on the collective states of gas in the galactic plane.

More precise constraints on the distribution of temperatures within isolated O VI components may be deduced from exact measurements of line shapes, which, when combined with data from other ions such as S IV, S VI and N V[7], may give an insight on the dominant regimes where heating and cooling take place. The sound speed in a general medium at the O VI-producing temperatures is about 80 km s^{-1}, and in a truly intercloud environment the turbulence from shocks reflecting off of clouds may stir up the material and make it harder to detect. This may explain why there seems to be too little O VI for the amount of soft x-ray and EUV emission seen in the local medium, if we wish to rule out the existence of both extraordinarily high pressures ($p/k \gg 10^4 cm^{-3}K$) and small filling factors for the hot gas. Thus, an important goal for IMAPS is the chance of discovering an additional source of O VI-bearing gas with an extraordinarily high velocity dispersion which may have been overlooked in the *Copernicus* survey because of the limited range of λ scanned for each line.

Finally, still another possibility is that for very hot and luminous stars, IMAPS may reveal some components which may be linked with conductive zones between expanding, radiatively cooled circumstellar shells and the shocks produced by

---

[7]The N V doublet at 1240Å is within the wavelength coverage of *HRS*.

strong stellar mass-loss winds, as described in a theory on "interstellar bubbles".

5.4. Dynamics of Interstellar Shocks

OBJECTIVE: to perform detailed mapping of high-speed components so that we can better understand the properties of violently disturbed gas and the structure of recombining and cooling gas behind shock fronts.

Recent observations and theories have emphasized the importance of shocks from supernovae, and the secondary disturbances which follow, as a source of motion and heating for the interstellar medium. The notion that these shocks can propagate great distances with relative ease seems theoretically plausible and is supported by observations of extensive systems of high velocity gas in the general vicinity of known supernova remnants and O-B associations (e.g., the Vela remnant, Orion association, η Carinae). Original blast waves in a low density medium may appear in the form of weak, high velocity (300 - 500 km s^{-1}) O VI features in spectra recorded by IMAPS, and if the gas is not preionized, shifted Lβ absorption from trace amounts of neutral hydrogen may be also present. Only very marginal indications of such features were derived by the *Copernicus* investigators, since they were hampered by the need to invest a large amount of observing time to scan a broad velocity interval with high photometric accuracy (the simultaneous imagery of many spectral elements by IMAPS greatly improves our efficiency for locating spectral features at unknown velocities).

As the high speed shocks encounter dense interstellar clouds, they slow down and the temperature of the post-shock material is reduced to a range ($T \approx 10^5 K$) where radiative cooling is important. At this stage many elements, such as C, N, S, Si and Fe, will have a significant fraction of doubly ionized atoms and will be very conspicuous in the spectral coverage of IMAPS. IMAPS will be able to distinguish

narrow absorptions from wide ones and hence will be able to differentiate high speed components which are photoionized (by stars or the radiation from the shock) from those components which are ionized and heated directly by the shock. Furthermore, we should be able to distinguish between the immediate post-shock gas, which travels at 3/4 of the shock velocity for $\gamma=5/3$, from the denser, cooling material which moves at the full shock velocity but at some distance behind the front. For sulfur atoms, IMAPS can display the profiles of four ionization stages. Hence we can map the recombination of the cooling gas as its velocity is changing and obtain a cross section of the shock's temperature structure. Also, by studying the lines of different elements, again as a function of velocity, we may witness the destruction of dust grains behind the shock as the normally depleted species shift toward the solar abundance ratios.

5.5. The Local Interstellar Medium

OBJECTIVE: to identify weak components produced by a very small cloud of warm, partially ionized hydrogen surrounding the Sun and study the interaction of this material with the surrounding hot medium which is probably at a much higher pressure.

From the backscatter of solar H and He emission line radiation, we know that our solar system is drifting at about 20 km s^{-1} through a partly ionized volume of gas having a temperature of about 10,000 K and a density $n \approx 0.1 cm^{-3}$. Absorption line measurements to very nearby stars by *Copernicus* and *IUE* indicate that this region is not too large; its edge is probably only 3 to 10 pc away. From analyses of the smoothly distributed soft x-ray background, there has emerged a consensus that we (and this local HI cloud) are probably surrounded by a volume of hot gas with $T \approx 10^6 K$ and $p/k \gtrsim 10^4 cm^{-3}K$ which extends out to about 100 pc. This

large, hot region may have been created by a supernova which went off not too far away some 150,000 years ago.

As a result of the gross pressure mismatch between the local H I gas and a newly created hot environment, there is probably an isothermal shock eating its way toward us from the cloud's periphery and traveling at a velocity equal to $[p_{outside} / p_{inside}]^{1/2}$ times the local sound speed of 10 - 15 km s^{-1}. To observe this shock over all (or most) directions in the sky with IMAPS would not only confirm the picture just described, but would also allow us to probe one particular example of a cool-cloud/hot-medium interface and learn more about the physical processes which occur therein. Such information would be of tremendous value to global theories on the creation and mutual interactions of various phases of the interstellar medium, such as that proposed by McKee and Ostriker in 1978.

Finally, *Copernicus* scanned the L-α emission profiles from the chromospheres of nearby, late-type stars. Absorption features from interstellar atomic hydrogen and deuterium are superposed almost on top of the peaks of these profiles. Unfortunately, at the resolution of *Copernicus* it was fairly difficult to know precisely what the shape of the emission profile would be without the interstellar absorption, so the inferred H and D column densities were rather controversial. The factor of 10 better resolution of IMAPS should help enormously to unravel the details of how the observed emission and absorption profiles really behave. These observations could be done starting at the L-β emission line, and the weaker, higher order Lyman lines could be used to check the conclusions.

6. PAYLOAD DESIGN AND PERFORMANCE

6.1. Mechanical Collimator

The mechanical collimator is composed of a stack of precisely coregistered electroformed grids, with each grid containing an array of square apertures (waffle pattern). The 1° wide (FWHM) triangular response in both directions on the sky, shown in Figure 4, prevents both the zero-order and diffracted light of all but the very closest interfering stars from contaminating the spectrum of the desired target star. The collimator aperture is approximately elliptical in shape, with semi-axes of 7.4 and 9.6 cm.

Direct light transmitted by the collimator has been measured to be 62% of the incident flux. Some of the energy loss can be attributed to the inevitable blockage of the beam by the opaque parts of the grids; diffraction and the resultant wide-angle scattering of light from the main beam account for the remainder. Undesirable effects from the cross-shaped array of diffraction spikes in the image format are reduced by having pseudorandom offsets in the spacing between the vanes (to eliminate coherent addition of phases which tend to make the pattern more "spiky"). The brightest (innermost) diffraction peaks each have an intensity of only 0.25% that of the main beam. To keep these spikes off of adjacent portions of a particular echelle order, the axes of the collimator's grid pattern are oriented 45° with respect to the dispersion direction.
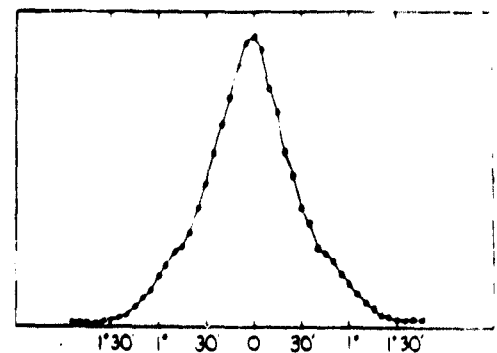

Fig 4 — Measured Angular Response of the IMAPS Mechanical Collimator

6.2. Echelle Grating

The echelle grating is a replica of an existing B&L grating ruled over a 200 × 400 mm area at 79 grooves mm^{-1} with a blaze set at tan θ = 2. Measurements at visible wavelengths show that this particular grating has very low scattered light and ghosts. An important feature of our design is that the incidence and diffraction angles are equal, with the two beams being offset on either side of the plane perpendicular to the rulings by a small angle (3.5°). This configuration insures that movement of the spectrum caused by either attitude changes (errors in ACS pointing) or thermal bending d'stortions of the payload ("hot-dogging") are tracked precisely by a broad-band reference image of the target star on the image format. Both the echelle grating and the cross-disperser (described below) were coated with Aluminum and a special overcoat of LiF designed to give good reflectivities at the desired wavelengths covered by IMAPS. The free spectral range of the echelle orders on the detector's image plane is about 4 times the width of the CCD. Thus, to obtain complete wavelength coverage, we provided a capability to tip the echelle in 4 different positions and make separate exposures in each case.

6.3. Cross-disperser Grating

The cross-disperser grating was specially ruled in 8.5 partitions on an off-axis paraboloid blank for the existing (sounding rocket) version of IMAPS by Hyperfine, Inc. This grating works in a Wadsworth configuration and focuses an image of its first order of diffraction on the detector at a distance of 1600 mm.

For sounding rocket flights we depend on thermal inertia and the short duration of the mission to insure that temperature changes will not appreciably alter the focus adjustment of the cross disperser.[8] For Spartan missions we will

---

[8]Actually, we intentionally set the ...us to be correct for some approximately elevated temperature, in anticipation that some of the aerodynamic heating from the hot outer skin would be transferred to the metering support structure of the instrument -- see the discussion in §7.3

circumvent the possibility that thermal excursions will throw our instrument out of focus by installing an invar metering rod between the cross-disperser and the detector and allowing the detector to move on a special mount (the distance between these two elements is the only critical dimension in our payload, light beams elsewhere in the payload are all parallel). Ordinarily, lateral movements of an image, caused by differential flexure of optical supports, can be a problem for standard spectrometers because they cause image smearing or result in an image drifting off a slit. For IMAPS, such motions are of no consequence because, as discussed earlier, the resulting errors look exactly like pointing errors which are compensated out by an on-board data processing system. In general, we feel that our optical bench can tolerate a thermal environment similar to that specified for the SAO invar spectrometer aboard Spartan 2, or perhaps even worse: first-order calculations seem to indicate that an overall temperature excursion of 40° C would be needed to throw our $f/10$ beam appreciably out of focus.

At the center of the detector format the geometric images formed by the cross-disperser should theoretically be perfect, but there will be some image blur from coma at the field corners. Ray-trace analysis indicates that the *maximum dimension* of the blurred image in the dispersion direction will range from 17μ to 22μ (perpendicular to the dispersion, the blur may reach 30μ at the very worst). Our estimate that the FWHM of the instrumental profile will be around 30μ includes this effect plus a pessimistic allowance for possible aberrations induced by mounting stresses on the gratings or defocusing caused by any residual lack of temperature compensation.

6.4. Detector

As emphasized in §4.1, short-wavelength photons must be allowed to reach the photosensitive medium without having to penetrate any sort of window, since bulk pieces of even the best optical substance (LiF) are virtually opaque to such radiation. Indeed, it is for just this reason that such general-purpose, uv observing facilities as *IUE* and the (first generation) spectrographs aboard the *Hubble Space Telescope* are unable to operate over nearly all of the very profitable wavelength range covered by IMAPS.

The IMAPS spectrograph casts its image onto a photocathode which consists of a layer of KBr on a solid substrate exposed to the vacuum environment. The quantum efficiency of an opaque photocathode of this type, approximately 77% near the middle of our spectral coverage, is markedly superior to that of the conventional semitransparent variety. Quite simply, this gain results from our being able to avoid the usual dilemma of making a semitransparent photocathode thin enough to allow the electrons to escape, while at the same time insuring that it is thick enough to interact with most of the arriving photons.
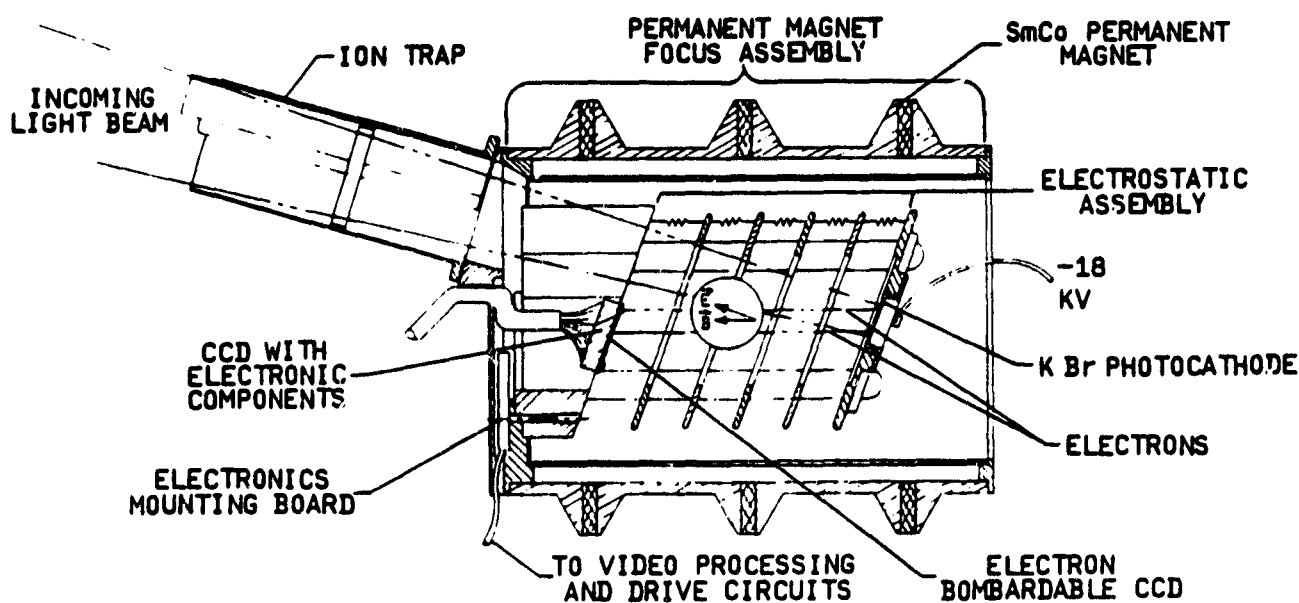

Figure 5

Inside the IMAPS ICCD image section, electrons emitted off the front face of the photocathode are accelerated by a 19 kV potential toward an RCA (SID-501) CCD with 320 × 512 separate charge collecting wells, each with a square dimension of 30μ. As illustrated in Figure 5, a magnetic focusing field is inclined to the voltage gradient by a small angle (20°) to allow the electrons to diverge from the optical beam and hit the CCD. From laboratory tests using a patterned photocathode (shadow evaporated through a standard Air Force bar-chart test pattern), we have verified that the oblique focus arrangement for the electrons produces as sharp an image as the CCD is able to show us. Theoretical calculations of the focusing properties of the oblique configuration give a 6μ diameter for the electron spot emitted by a single point on the photocathode.

So that it can respond to direct electron bombardment, the CCD has its normal supporting layer of cover glass etched away. Upon impact, each high-energy electron produces 3 to 4 thousand secondary charges in the CCD's silicon layer. The entire field of the CCD is read out 15 times a second, and a display of the frame clearly shows photoevents as large spikes, spread over one, sometimes two, and very occasionally three or four CCD wells (depending on whether or not the incident photoelectron landed near a well boundary). It is not necessary to cool the CCD, because not very much dark current is accumulated over the 1/15 second duration of an exposure. The ratio of an event's charge to the noise in a single well is about 35 to 1. With this large a signal margin, we are very confident that we can resolve the position of a hit to within half of a 30μ CCD well, by analyzing the charge centroid. (This is a conservative estimate for positional accuracy; theoretically we should be able to do even better.) The resulting sample interval of 15μ is fine enough to avoid aliasing problems with the spectral information (unless the image quality is much better than we predicted).

If ions enter the ICCD image section, or are created therein, they are accelerated toward the photocathode. When they hit, they each produce a bunch of electrons (about 10 or 20 in number) which will, in turn, register as a great big event on the CCD. As long as these ions events are not so numerous that the detector field becomes much too busy, we can make them have virtually no influence on our observations because they are easily recognizable (because of their large amplitude) and can be rejected by the event-detection processing by a computer after flight. In our laboratory vacuum tests of the IMAPS ICCD, we found that the ion event rate was very low (only a few events per 1/15 second frame), and there was very little increase when we deliberately let the pressure degrade to 2×10^{-4} torr. Likewise, on the successful sounding rocket flight, the ion rate was very low (see §7.3.1.6).

The low ion rate we experience with the detector is probably attributable to a number of precautions that we have built into the design. First, the optical system and the detector are enclosed in a cylindrical vacuum vessel which is always pumped down for a long period of time before flight. This pumpdown virtually eliminates outgassing from adsorbed volatiles or trapped gases (within small voids) inside the payload. As a second precaution, we installed an ion trap in front of the detector and put the mechanical collimator (the only opening to the outside) at a slightly positive potential with respect to the outer shell of the payload. Finally, we have found from our laboratory testing that the most important parameter for keeping the ion rate low is cleanliness of the payload components, especially those associated with the image section. In recognition of this, we thoroughly cleaned and vacuum baked the ICCD assembly.

6.5. Signal Transmission

For sounding-rocket flights, we amplify the raw video signal from the CCD, package the information into the standard broadcast TV signal and synchronization protocol (but with each CCD row expressed in 4 TV lines and 2 TV frames per CCD frame), and then telemeter the signal to ground for recording on a VCR tape. After flight, the video recordings are digitized and photoevents are subsequently recognized and centroided by computer processing. While this extremely simple approach has been suitable for observations of short duration on a vehicle which can transmit wide-band telemetry, we will need to adopt a more elaborate approach for our Spartan flights. None of the tape recorders proposed for Spartan have the capacity to store a standard TV broadcast for a whole flight; thus we will need to create an on-board processing system to carry out the event analysis in real time and thereby consolidate the information into many fewer bits.

6.6. Compensation for Small Pointing Errors

On rocket flights, there is no active system to stabilize the wandering of a spectrum while the rocket's attitude moves within the ACS limit cycle. Instead, a small mirror[9] ($\sim$1 cm^2 in area) attached to the echelle grating directs a broad-band image of the target star to the cross disperser which in turn focuses it near one edge of the ICCD picture format. As the spectrum moves in x or y, this bright, point image moves in precisely the same manner (see §6.2), and we use it as a position reference in each recorded frame. As long as the rate of angular motion is less than about 5″ s^{-1}, the smearing of spectral detail in a single 1/15 second frame will be completely negligible (a 15μ sample is equivalent to 1.72″ in the sky).

[9]There are actually 5 such mirrors installed on the echelle housing, one for each of the 4 tip positions and an extra one on an opposite side of the echelle to serve as a focus monitor in one of the positions.

Even the worst angular rate quoted for the Strap 5 ACS (10″ jitter peak to peak ⊚ 0.2 Hz ≡ 4″ s⁻¹) is within this tolerance.

7. TECHNICAL HIGHLIGHTS

In the following sections, we cover a number of key technical issues which contributed to interim successes and failures within the IMAPS program. These topics are presented here for two reasons: (a) They had a major impact on the program schedule and cost and also the realization of certain technical and scientific goals, and (b) they cover important findings which reflect on the overall capabilities of the IMAPS instrument and associated subsystems.

7.1. Problems with CCD Performance

In preparation for its first flight, in February 1983 the IMAPS payload underwent the standard integration and evaluations at GSFC (e.g., tracker alignment, electrical functional tests, determination and adjustment of the center of mass, bend tests, spin balancing vibration tests and post-T&E integration). In addition, we evaluated signal transmission quality of our ICCD output throughout the telemetry system. Overall, the outcome of the GSFC integration tests were uneventful, and the payload was successfully integrated with the rest of the rocket systems.

After the integration run at GSFC, we transported the payload to the Naval Research Laboratory (NRL), where G. Carruthers had a test facility which permitted us to evaluate the performance of the complete payload assembly for imagery of spectra. The intent of this test was to determine how well the optical system formed a spectral image. Major items for the test were a) whether or not the collimator had objectionable diffraction spikes, b) How efficient were the optical components, c) how much scattered light came off the gratings, d) a double check of

the focus, and e) a full-up test of the signal processing chain.

After about five days of intensive testing and problem solving, we ascertained that the payload had an enormous loss of sensitivity. We could detect a signal only when the test apparatus was emitting a flux far above what we could ever expect from a celestial source. At the time, we were unable to determine whether the problem was relatively trivial, such as from a simple mechanical interference in the beam or a grating being off its blaze, or more fundamental, such as an insensitive detector or nonfunctioning optical component. Since it was clear that we could not fly the instrument under the circumstances, we postponed the flight and shipped the payload back to BASD for trouble shooting.

Our initial suspicion was that there was no fault with the CCD, because we thought we were able to register the presence of individual photoelectrons and our problem was simply that there were few in number (that conclusion, as later investigations revealed, was definitely false!). Thus, in the early phases of trouble shooting, we concentrated on possible sensitivity losses in the optical system and/or photocathode.

After its arrival at BASD, the payload was inspected and found to be basically sound. Next, the alignment of the optical system was verified, and a special test was performed to check that the grating blaze angles were indeed where we expected them to be. With those evaluations showing essentially no problems, we embarked on the more difficult task of checking the efficiency of the optical components. To accomplish this, we fabricated a special fixture for directing a beam of light from a uv source first directly onto the detector, followed by a new setup with the assembly illuminating the detector through the complete optical chain. As is usually the case with measurements of optical efficiencies, fairly elaborate precautions were needed to insure that systematic errors of various sorts did not give us invalid readings. Various practical problems, such as electrical

interference from a noisy power supply for the uv lamp, prevented us from obtaining very definitive quantitative data on the optical efficiency. However, from rough comparisons of the results from the two illumination schemes, we could satisfy ourselves that the optical system in the IMAPS payload could not alone be the explanation for our overall efficiency problem (i.e., several orders of magnitude below a calculated efficiency for the whole system).

After the tests of the optical system, our attention turned to locating possible deficiencies of the detector. From previous tests of electron yields from single photoevents, measurements of the CCD on-chip amplifier gains, and our experience with the random noise at the output, we would have predicted that single photoevents would have had a healthy 20:1 signal-to-noise ratio. On the other hand, examination of the recorded data showed that the photoevents were not too easily recognizable, and in addition, they seemed to show a large dispersion in amplitudes. In one diagnostic session with the camera electronics, we discovered an open circuit in the CCD amplifier reset line, caused by a wire which had come loose from a connector. After correcting this problem we found an improvement in the recognizability of events, but the overall sensitivity of the detector had not improved. G. Carruthers remeasured the quantum efficiency of the photocathode at NRL. While some loss of efficiency had occurred, it was only by a factor of three at the very most -- far short of the amount needed to explain our sensitivity problem.

The complete ICCD detector and associated electronics were shipped to Princeton for further study. In support of another research program at Princeton (evaluation of ICCD detective quantum efficiencies), we had on hand a uv source whose absolute flux had been calibrated. It consisted of a radioactive source which produced Cerenkov light in a MgF_2 crystal at the focus of a collimating mirror. The yield from the source should have produced 400 events per second over the

complete ICCD frame area, yet we were unable to see any events whatsoever, when we viewed the video output on a monitor screen. Ultimately, this test convinced us that our fundamental problem rested with the apparent inability of the CCD to show us *single* photoevents. In the past, we thought we could see such events when the detector was exposed to bright uv sources. However, these sources were so bright that what we were indeed seeing (and interpreting as single events) were the chance pileups of multiple electron hits on top of a crowded sea of photoevents.

This conclusion was surprising at the time, since, at least superficially, straightforward calculations of the overall sensitivity seemed to indicate that we would have had no difficulty in registering single events. Specifically, we knew that from previous experiments with the CCD operated in slow-scan mode (long integration times, CCD cooled to -130°C, 10 second readout time for a whole frame) that the charge yield for 17 keV electrons was about 4000 electrons per event. The charge sensitivity for the on-chip amplifier at the high bandwidths needed to record at the IMAPS fast scan rates was $0.25\mu V/e^-$ when it was connected to a 3KΩ load of the IMAPS video amplifier. While this gain was lower than the nominal value of about 0.5 to $1.5\mu V/e^-$ found for this and similar RCA CCDs, by itself this reduction could not explain why we were unable to see events. An additional effect, however, conspired to reduce our signal margins farther. From experiments at slow-scan rates with several different CCDs viewing an optical test pattern, we knew that pulses only one pixel wide experienced a loss of signal amplitude by about a factor of two, compared to illuminations which covered a large number of contiguous pixels. Even so, we calculated that 17 keV charge packets passing through the IMAPS signal chain with its gain of 560 would produce pulses with an amplitude of 280 mV, if all of the charge were concentrated in a single pixel. Compared with measured rms noise levels ranging from 24 to 36 mV, we expected a signal-to-noise

ratio somewhere between 8 and 12.[10] While this was ostensibly a reasonable margin for detection, we nevertheless harbored an awareness that, at the higher clocking rates needed for IMAPS, any further reductions in the CCD's charge transfer efficiency (CTE) could compound the attenuation of point-like signals and jeopardize our ability to perceive the events.

Following these initial conclusions, we embarked on an intensive evaluation of many different CCDs. Our goal was first to obtain a better perspective on the limitations of then currently available devices and then explore what corrective actions we could take to restore the IMAPS ICCD to a condition where we could unquestionably record individual events. As a first step, we tested two CCDs purchased for another NASA grant program at Princeton (for an optical observing camera for ground-based telescopes). These CCDs, virtually identical to the RCA type 50[1] scientific chips selected for the IMAPS detector, were assemblies mounted on glass (hence they were not electron bombardable).

While both devices showed good responsiveness in their on-chip, dual stage output amplifiers, 1.5 $\mu V/e^-$ for one device and 1.4 $\mu V/e^-$ for the other (which was a major improvement over the earlier 501 chip designs), they still had rather poor parallel CTE, even after we had experimented with changes in the rise and fall times of the vertical (parallel) clocking waveforms. For both chips the CTE was bad even at high signal levels or during operation at -80 °C (often, CCDs show poor CTE only at low signal levels and low operating temperatures; the problem usually clears up for strong signals). Specifically, the poor CTE degraded a spot

---

[10]This criterion for signal-to-noise ratio is a standard that we have adopted, even though the actual instantaneous signal level above the noise may be less when the charge is spread over two or more adjacent pixels. This measure has been used as a gauge for the effectiveness of event detection strategies and assessments of the minimum performance we needed from the ICCD and the subsequent signal processing and amplification chain. In the absence of intangible difficulties, we calculated that we could pick up events with a SNR of about 7 without any appreciable overlooking of valid electron hits, while at the same time we wouldn't register an appreciable number of spurious events from the inevitable large noise excursions.

illumination of a single pixel with a level of 12,000 e^-/pixel to a point that it couldn't be seen above the noise on a repetitive oscilloscope tracing of a single line's readout. This pixel was located near the center of the field. Another pixel near the top of the A register which was illuminated with the same single-pixel spot couldn't be seen until the signal went above 21,000 e^-/pixel! The appearance of a bar-chart test pattern indicated that the serial CTE for these devices was alright however. We also noted that the readout noise levels were a bit on the high side: one device showed a noise of 200 e^- rms in the active pixels and 160 e^- rms in the overscan area, while the other showed respective values of 150 and 130 e^- rms. These CCDs were eventually returned to RCA because we felt that they were unsatisfactory.

After the above mentioned tests were completed, it became clear that major improvements in CCD performance were needed to achieve our objective of registering individual electron events at the IMAPS frame rates. In the summer of 1983, we were informed by RCA that a new design of CCD would be produced which, they claimed, would have somewhat better performance. We responded by placing an order for this new device, with a specific request that it have the cover glass chemically etched away so that the CCD would be electron bombardable. At the time, we were informed that the new CCD would be shipped several weeks after we placed the order. As things turned out, however, it didn't arrive in Princeton until early December of that year. This delay in the procurement created a significant slip in the IMAPS program schedule.

As with the two CCDs used for ground-based observing, the amplifier exhibited good gain ($1.3 \mu V / e^-$) but with this device the serial CTE was not especially good. In contrast to the earlier two chips, however, we found that the CTE was alright with moderately large signal pulses, or with small signals on top of an elevated zero-level background (around 25 mV). In fact, with a signal bias from the high

dark current that we could anticipate for normal fast scan operation at room temperature for the IMAPS camera, we ascertained the CTE would be acceptable, that is, individual photon events would not become unrecognizable. The noise level in slow scan operation was equivalent to 110 e^- rms, which for IMAPS operations was a good figure. One disturbing feature of this particular CCD was that its quantum efficiency showed strong variations over the field. A flat field exposure showed global fluctuations of about 50% in amplitude. While this probably would not present a serious operational problem for IMAPS, the lack of uniformity indicated that there might have been some problems with quality control in the manufacturing process.

Shortly after the evaluations of the first new IMAPS CCD had begun, we had the opportunity to check out a much newer CCD purchased by the image sensor development group at Princeton's Plasma Physics Laboratory (PPL). This CCD was from a brand-new batch produced at RCA. We learned from RCA that this newest batch had some processing improvements incorporated into their manufacturing procedures. It was immediately apparent to us that the PPL chip was significantly better than any chip we had seen before. The CTE for this chip was excellent all the way down to signals of 1000 e^-/pixel (single pixels could be seen at that level). A surprisingly high gain of 2.6 $\mu V/e^-$ was found at the output of the amplifier, and the noise was only 60 e^- rms. The response to a flat field illumination was quite uniform, and there were no blemishes, hot pixels or bad columns. Another very extraordinary feature of this chip was that the dark current was quite low. In the slow scan test set, which normally clocks out the CCDs at a rate which gives an effective integration time of 10 seconds per frame, the dark current at room temperature gave a charge equal to only 3/4 of the full well capacity of the pixels!

On the basis of the very favorable results we obtained for the PPL CCD, we decided to place immediately a new CCD order for the IMAPS program. We were especially anxious to obtain a device from the same production run as that which

generated the device which belonged to PPL. Also, we felt that it was important to have a backup chip to support our flight operations.

The second IMAPS chip arrived in Princeton in mid January of 1984. Much to our delight, we found that the slow-scan performance of this chip seemed to be about as good as the PPL one. The noise was only about 90 e^- rms, and once again the thermal dark current seemed extraordinarily low at room temperatures. Both the serial and parallel CTE at slow scan seemed to be excellent. We had no trouble seeing a single pixel illuminated at a level of 2000 e^-/pixel, which is a weaker spot than we'd expect from single 15 to 20 keV electrons in the IMAPS ICCD. The sensitivity of the output amplifier was again as good as we had seen in recent CCDs from RCA: 1.4 $\mu V/e^-$. Also, a very clean format with a uniform flat field response was observed.

When we installed the new CCD in the IMAPS breadboard fast scan camera system, we   were pleased to see that the charge sensitivity of the output stage was, as close as we could determine, as good as the slow-scan performance. This was an important improvement over the CCDs which we had purchased much earlier for the IMAPS program However, the fast-scan testing also gave us a preview to some unanticipated technical hurdles. It was immediately apparent that the very fine CTE we could obtain at slow scan rates was no longer in evidence in the fast scan camera: in essence, things had really gone to pot! (We never experienced a loss of CTE going from slow scan to fast scan in our evaluations of CCDs in past years.)

After some inves·· ·tion, we determined that the source of this new CTE problem was indirectl·   ·sult of the new construction of the CCDs. To overcome the more fundamental lack of good CTE in their devices, RCA modified the construction of the gates from an open strip configuration to a more highly overlapping sandwich-type layout. This type of construction was intended to reduce the losses

resulting from field fringing at the gate boundaries when the phases were switched, and the excellent CTE we were finding at slow scan rates confirmed that the new design strategy was working well. However, a byproduct of the new construction was that the interelectrode capacitances were significantly higher than in the old design. As a consequence, with our current electronics we were unable to impose properly shaped waveforms on the input pins of the clocking gates. Based on advice we received from RCA Laboratories, we concluded that the high capacitance resulted in a bad impedance mismatch through the 3 or 4 inch leads between the clocking output drivers and the CCD. They advised us that leads longer than an inch or so were bound to give us difficulties in obtaining the necessarily sharp waveforms to do really fast transfers. Also, the output driver stages in our camera didn't seem to have enough current capacity to do the job. We experimented with shorter lead lengths and extra emitter follower stages to help us obtain better waveforms at the CCD and hence improve the CTE, but only a mild improvement was seen.

While we could have gone to more extreme measures to improve the clocking drives and physically relocate the circuits, such changes would have forced us to do a major rebuilding of the flight camera. The modifications would have entailed our putting the output driver stages very near the image section -- an undesirable option in view of the probable outgassing from the circuit elements which are dissipating a large amount of heat. Even then, we judged that there might still be some risk that we would be operating the chip clocking under marginal circumstances. In the light of this, and again following the advice from RCA, we decided that the best course of action was to relax on the whole timing scale and reduce the overall frame rate of the IMAPS camera by a factor of two. Thus, we would operate the camera at 15 frames per second instead of 30. Indeed, when we experimentally reduced the master clock frequency by this factor of two in the

breadboard camera, we were able to clock the CCD much more comfortably, and the good CTE returned.

Reducing the frame rate had both some advantages and disadvantages. The primary disadvantage of having a longer integration time per frame was that the maximum permissible count rate was reduced by a factor of two, if we wished to identify individual events. At high photon flux levels we would still be able to properly sense the signals in an analog fashion, but event confusion would preclude us from going beyond our nominal wavelength resolution ($\lambda/\Delta\lambda = 2\times10^5$) by means of centroiding (i.e., by obtaining sub-pixel resolution).

Another disadvantage of the slower frame rate was that the image smear due to angular motions of the rocket in the ACS limit cycle would be doubled. This didn't appear to be a serious problem, since at 30 frames per second we had a generous margin of safety, even if the ACS motions were as high as 15 arc sec per second of time. Even though the safety margin was to be reduced by a factor of two, it still seemed acceptable.

An important *advantage* of going to a slower frame rate was that the dwell time per pixel during readout was increased, which meant that the bandwidth requirement on the telemetry system and our recording apparatus could be relaxed. In other words, we could experience a reduction by a factor of $\sqrt{2}$ in the noise per pixel attributable to losses in the signal link between our amplified video output on the payload and the eventual post-flight digitization for the data reduction computer on the ground. We felt that this was an important consideration. Finally, a minor advantage of going to the slower frame rate was that we could expect to have half as many image frames to process on the ground. At the present moment (when this report is being written), this factor is most prominent in our minds, inasmuch as we are arduously making our way through the some 5,000 frames of data from the most recent flight of IMAPS!

In summary, we felt that our position *vis-a-vis* CCD performance had improved markedly over our situation of approximately a year earlier, when we discovered that the IMAPS instrument sensitivity was falling far short of our expectations. The new RCA chip design had a number of important improvements which reflected very favorably on our ability to detect single high-energy photoelectrons in the IMAPS image section:

[1] The single level gate electrodes were replaced by multilayer, overlapping gate structures to improve the CTE.

[2] The single video output transistor on the chip has been replaced by two amplifiers working in cascade. This resulted in a more predictable output response (from one device to the next) and seeed to prevent the signal loss which occurs when the sample times are shortened (at fast scan) or when the output impedance is lowered (the input impedance of the IMAPS camera circuits was only $3K\Omega$). At fast frame rates the improvement in charge sensitivity seemed to be about a factor of 3 over the earlier devices. Also, the readout noise, expressed in terms of equivalent electrons per pixel, was about a factor of two lower in fast scan applications.

[3] Better manufacturing procedures or higher quality silicon in the new CCDs evidently gave us devices with very much lower thermal dark currents and formats which have very few cosmetic problems. The flat-field response also seemed to be excellent. While these considerations were not too vital for IMAPS applications (aside from making the data reduction a bit easier), they indicated that the overall quality of the product had improved, which probably also reflected favorably on its survivability.

[4] Some of the signal lines leading to and from the on-chip amplifier had better shielding from the clocking leads. As a consequence, the instantaneous levels detected by the IMAPS sample-and-hold modules were less subject to

interference from the tails of the clocking pulses. We later realized that this change gave us a vastly lower response to interference from noise pulses from the voltage regulators in the electronics power supply. Evidently, the carry-over of the pulses into the video signal was caused by part of the video sampling riding up on the steep exponential tails of the previously enormous clock pulses in the CCD's raw output.

[5] The new CCDs had a much better pin design. We could expect to see a significant improvement in the reliability of the electrical connections to the device, especially under the severe environmental conditions of a rocket flight.

7.2. First Flight of IMAPS on a Sounding Rocket (27.071UG)

The first launch of the IMAPS instrument on a Black Brant rocket occurred on October 5, 1984 at the White Sands Missile Range. The target star chosen for this flight was ε Perseii. This star is especially important to observe in the ultraviolet with an instrument having good spectral resolution, since earlier *Copernicus* data indicated that there are about 5 separate components in the interstellar medium along this particular line of sight. With spectra taken at the velocity resolution of *Copernicus*, these components are badly blended, and their existence was known only by careful modeling of the smeared profiles.[11] Far more definitive results would be forthcoming if these components could be untangled. Interstellar results for this star are also enigmatic: Vidal-Madjar *et al.* [12] found that the apparent ratio of atomic deuterium to hydrogen varied with the time of observation (typical time spacing of about a few hours).They explained this in terms of effects from time-variable winds from the star. Since *Copernicus* scanned different lines at

[11]Martin, E. R. and York, D. G. 1982, *Astrophysical Journal*, 257, 135.

[12]Vidal-Madjar, A., Ferlet, R., Laurent, C., and York, D. G. 1982, *Astrophysical Journal*, 260, 128.

different times, they found it very difficult to unravel the true differential equivalent widths for lines of D and H from the perturbations caused by the stellar wind on the blue-shifted component. Observations by IMAPS could unravel this mystery, since all wavelengths would be observed simultaneously.

Except for some difficulties with payload testing at NRL prior to our going to the Missile Range for the launch, preparations for the flight were uneventful. At NRL, when we attached the IMAPS instrument to Carruthers's vacuum tank and collimated ultraviolet source, we once again found the payload had a drastically reduced sensitivity (initially, it seemed as if we were repeating our unpleasant experience the last time we tested IMAPS at NRL! -- see §7.1). After several days of troubleshooting, we discovered that the echelle grating was not set at the correct angle. This improper setting meant that we were observing light far from the grating blaze angle. During optical alignment at BASD, there had not been a realization of the importance of having this angle set exactly at the right value (the width of the beam is only about 1/2 of a degree because the grooves are very wide).

We corrected the grating angle by installing a shim on the attachment to the arm which rotated the echelle. Much of our difficulties in identifying this problem was attributable to our being unable to measure the alignment of the IMAPS optical axis relative to the collimator for the ultraviolet source. As a result of this experience, we took note of the importance of providing fixtures for measuring this alignment in future testing at NRL.

During the flight of IMAPS, there was a catastrophic degradation of the vacuum inside the instrument. As a consequence, the detector's high voltage underwent a continuous discharge during most of the observing time. The loss of vacuum and its effect on the instrument were indicated by three independent telemetry signals: 1) The readings from an ion gauge installed in the payload, 2) The initial lack of any high voltage level after the HV power supply was activated,

followed by a slow, ragged (from arcing) recovery, 2) Excessive current draw on the HV power supply, and 3) the CCD television signal which was solid white. Thus there was little question about the nature of the failure. The only mystery at the time was what was the cause of the inrush of air.

We now recount some of the significant events which happened during the flight. The prime anomaly, of course, was the breach of vacuum which must have occurred after T = 0 seconds. After the vacuum seal plug was inserted at T = -10 minutes, we monitored the vacuum inside the payload with our ion gauge. The leak rate was quite small, so we were satisfied that we had no problem whatsoever prior to liftoff. As a safety precaution, we turned off power to our payload at about T = -1 minute so that the vibration during the ride wouldn't accidently trip a relay or momentarily short something in our experiment (a timer in the instrumentation section restores power after burnout). Since the ion gauge ran on our experiment power, we had no record of when the leak occurred. After the power was restored at T = +62 seconds, the ion gauge indicated that the vacuum was horrible -- see Figure 6 (on page 49). After the aperture was opened, there was a nominal drop in pressure, but the pumping rate seemed to be very slow.[13] At T = 103 seconds, the ion gauge was programmed to shut down so that the detector could function without an ion background from the gauge.

After a while, the quality of the vacuum within the instrument chamber improved because of the pumping action through the entrance aperture. The high voltage eventually stabilized at the proper value, and the CCD went from solid white to a condition where one could see an avalanche of ions hitting the photo-cathode. After about T = +420 seconds, the ion rate subsided to the point where genuine photoevents (i.e., a real signal) could be seen. Over the interval from +420

---

[13]The small uptick in pressure on top of the decay occurred at precisely the time the ACS valves fired for the main maneuver to target.

to +472 seconds, the detector was registering a complicated mixture of residual ions (which produce very strong signals) and true photoelectrons. The altitude of the rocket at that time was still high enough to allow IMAPS to view an ultraviolet spectrum from ϵ Per.

It is conceivable that there is useful data buried amongst the clutter of ions. Careful extraction techniques with a computer might recover some scientific information. However in view of the much greater quantity and quality of data obtained from the subsequent flight of IMAPS (described in §7.3), the importance of committing time and resources to such an ambitious data reduction task has been diminished.

At the time, we had no indication at all where the failure of a vacuum seal occurred. The break seemed to have been only momentary, since there was a reasonably good vacuum present in the payload after it was recovered some 8 to 10 hours after the flight. The vacuum we found afterwards was consistent with atmospheric pressure at an altitude of about 30 km, which agreed with the altitude where the aperture door closed according to the radar tracking data (at T = +491 sec).

Our initial conjecture was that stresses from the powered flight must have jarred loose one of our O-ring seals somewhere. Of all the vacuum seals on the payload, we presumed that the most vulnerable one is that associated with the aperture door. However, this door has about 200 pounds of spring pressure to hold it closed, in addition to the force from the atmosphere which is about 900 pounds at sea-level pressure (this force is slightly lower at the elevation of WSMR). The force holding the door closed seemed to be pretty generous compared with the expected g-loads; the weight of the door itself is only about 1 pound.

There were two other significant anomalies which occurred sometime during the flight. One was a break which occurred in a weld where the outer skin (not the

vacuum vessel, but the load-bearing cylinder which surrounds it) joins one of the bulkheads. The break was complete along about 2/3 of the circumference. Fortunately, the break didn't go all the way around the skin, otherwise we would have had a real disaster on our hands (i.e., the payload might have been completely destroyed or at least seriously damaged).

The outer skin was provided to the project by the sounding rocket division at GSFC. Since much of the responsibility for sounding rocket mission operations was being transferred to WFC shortly after our flight, we returned the skin (inasmuch as it was GFE) to WFC for evaluation and repair. The weld was inspected at WFC and it was found to be defective (the bead had insufficient penetration).

The other major mechanical problem was that the detector assembly, weighing 31 pounds, had torn loose from its mount. Fortunately, clearances in the vicinity of the detector were so tight that it did not go crashing around inside the payload, inflicting damage on itself and other instrument components, such as the gratings or mechanical collimator. A shock in excess of 100 G's would have been necessary to shear the 2 1/4-inch dowel pins and 4 10-32 socket-head stainless steel cap screws which secured the assembly. A less severe stress could have broken the detector loose if an outer anchoring point failed before the others felt the load (i.e., a zipper type effect). There is no evidence from the accelerometer telemetry that a large stress occurred during the flight, but it is conceivable that the payload felt a significant shock when the entire package fell over like a tree after the initial impact on the desert.

Our corrective action for the next flight of IMAPS was to use stronger bolts to secure the detector assembly to its mount. The stainless steel cap screws were replaced with hardened steel screws of the same size, increasing the load capability by at least a factor of two.

In the months which followed the flight, we investigated various possibilities for the cause of the vacuum failure. The payload was inspected carefully for any evidence of physical damage that might indicate where the leak occurred. None was found. We tried to stress parts of the payload that could result in possible flexure that would cause an O-ring seal to fail, but we were unable to create a failure. Finally, we hypothesized that trapped air in some void within the payload's vacuum vessel could have been released under the shock and vibration of the rocket flight. We tried to simulate this failure mode by vibrating the payload to flight levels while it was under vacuum. No release of gas was detected while the vibration was in progress, beyond a barely perceptable increase in the normal leak and/or outgassing rate.

In summary, many months of thinking and tests failed to produce a definitive explanation for the vacuum problem on the flight. These tests could not definitely rule out some of the hypothetical causes, but we could not pinpoint a real problem area and make what we considered to be a definitive fix. Up to about a month before the second launch, we devised the following corrective actions which, we felt, would lessen the probability of the failure happening again:

[1] We increased the spring pressure on the aperture door to 400 lbs. While we felt the previous pressure should have been adequate, the extra force would give an extra margin, in case some strange vibration built up during the flight which caused enough warping or rattling of the door to cause the seal to fail. A change in the spring constant would also change its resonant frequency, which might also be beneficial if our previous misfortunes were the result of some buildup of vibration.

[2] Relief holes were drilled in all places inside the payload that were suspected of being able to trap air.

[3] We decided to vibrate the payload at White Sands *after* the vacuum can had been pumped down for the last time before flight. If there were any trapped voids containing air still within the payload (i.e., corrective action [2] above didn't get them all), they would be very likely to be relieved during this vibration on the shaker, rather than on the flight itself.

[4] A separate source of power was provided to the ion gauge, so that it could operate independently of our payload electronics whose supply was intentionally turned off during powered flight. If the failure reoccurred on the second flight, we'd have a better indication from the telemetry of when and how rapidly the failure occurred. On the first flight, all we could tell was that the vacuum was very bad at a time well after powered flight (but before the door had opened).

[5] Silicone potting material was applied over all joints on and near the ion gauge. The ion gauge was housed in a sealed can maintained at normal air pressure to keep its high voltage leads from arcing at intermediate ambient pressures. Since the pumpdown of the payload after the aperture door had opened was not rapid, we surmised that a slow leak from this sealed can could have disastrous consequences. The actual probability that this sort of failure really occurred seemed rather low, inasmuch as there was no leak near the ion gauge after the flight. Any breakage of the seal would have had to mend itself afterwards!

[6] We lengthened the time interval between the door opening and the activation of the high voltage power supply. This would give more time for the payload to pump down, if the pressure were too high at the beginning. (Once an arc is established, the pressure for it to be quenched is much lower than the minimum pressure to establish it in the first place.) The time interval on flight 27.071UG was 13 seconds; for 27.082UG it was lengthened to 20 seconds.

Also, the door opening was posponed to a higher altitude (later by 8 seconds, which made the altitude 142 km instead of 135 km on 27.071UG).

A significant breakthrough in our investigation of the vacuum failure occurred about two to three weeks before the second launch. During the testing of the payload's optical performance at NRL, Don Bradshaw (of BASD) happened to notice that the vacuum pump on Carruthers's apparatus was able to pump the IMAPS instrument through the front aperture much more rapidly than the rate of pressure decrease experienced on the first flight! In essence, a simple diffusion pump on a laboratory setup performed better than an ostensibly perfect vacuum pump with unlimited pumping speed (i.e. the vacuum of space at flight altitudes)! Figure 6 illustrates the tremendous disparity between the two rates (compare the curve labeled "test pumpdown at NRL IMAPS ion gauge" with that labeled "IMAPS I 27.071UG" after the door opened).

IMAPS FLIGHT PRESSURE PROFILES

27.071 UG   OCT. 6, 1984
27.082 UG   APRIL 20, 1986

FIGURE 6

STANDARD ATMOSPHERE

SEPARATION

DOOR OPEN

TEST PUMPDOWN
AT NRL
IMAPS ION GAUGE

NO DATA
POWER OFF

IMAPS II 27.082 UG

IMAPS I 27.071 UG

SEPARATION

DOOR OPEN

NRL ION GAUGE

PRESSURE IN TORR

10^{-1}

10^{-2}

10^{-3}

10^{-4}

10^{-5}

TIME IN SECONDS (LAUNCH AT 0)

-40   -20   0   20   40   60   80   100
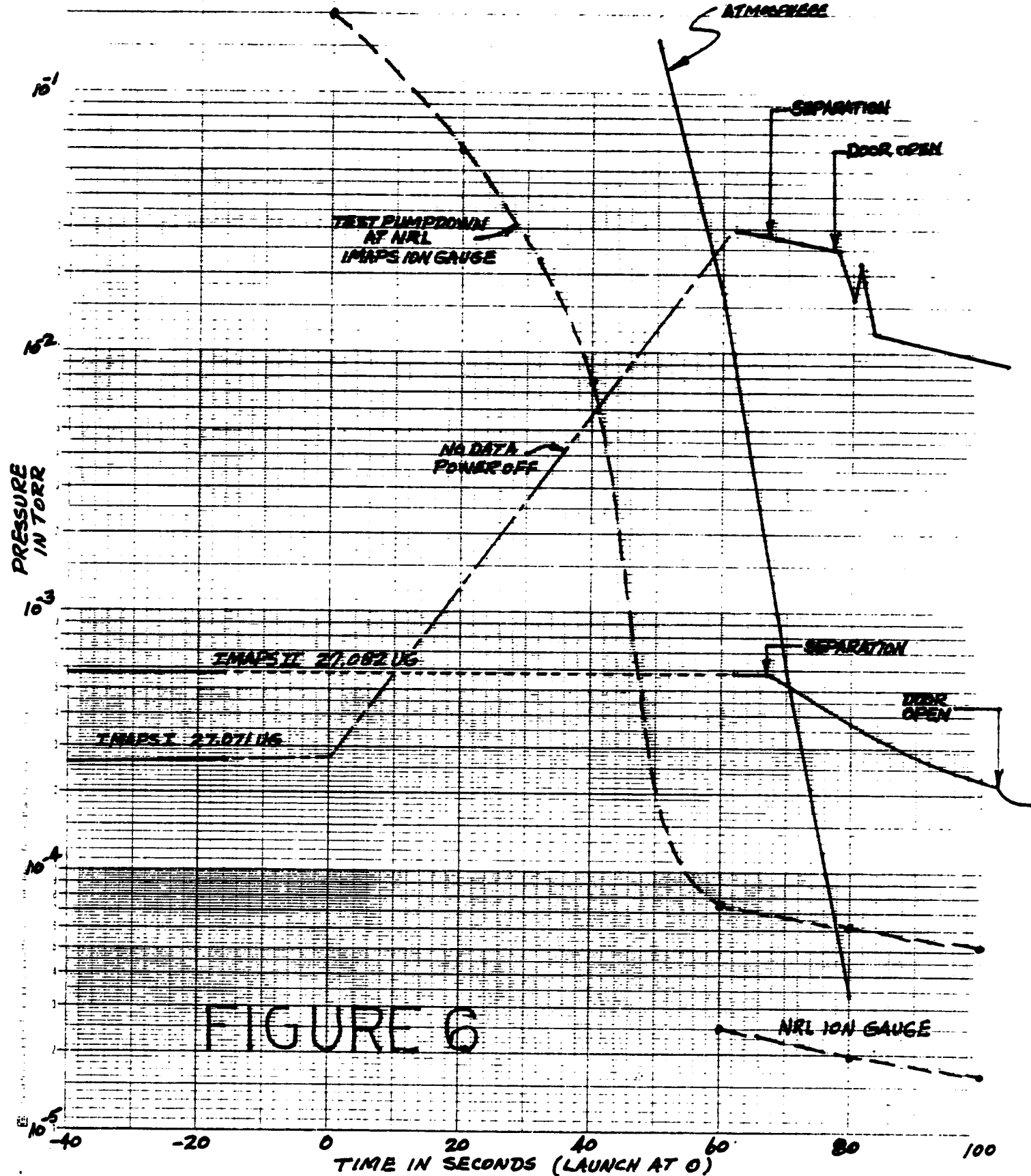
This finding gave us a clue that the sustained high pressure inside the vacuum can during the observing time was not caused by simply a large insertion of gas at some previous instant followed by a slow pumping rate through the mechanical collimator. *The long duration of high pressures was the result of a sustained leakage of gas, either directly into the payload or in its immediate environment.* With this insight as a strong hint, some further thought produced the following explanation -- one which we now think is the most probable description of the source of our vacuum problem: There was no intentional venting of the housings for the ORSA, ACS, telemetry, or experiment electronics systems. Since the operation of these systems in flight are unaffected by the pressure, that is, they could function perfectly well between a pure vacuum and one atmosphere pressure, no notice was taken as to whether they were perfectly sealed or were allowed to vent. As has been the practice on other flights, the chambers between the nose cone and the experiment were allowed to leak (very slowly) through joints in the skin (see Figure 7). Another way to relieve the pressure, however, was for gas to flow through the chamber which housed the experiment electronics, then through some narrow slots which provided thermal isolation on the rear support for the experiment vacuum can on the rocket skin, along the cylindrical void between the vacuum can and the skin, and finally, into the open housing *right in front of the viewing aperture of the instrument!* We feel that a partial retention of gases by this housing before they vented into space could result in an appreciable influx of molecules into the payload.

NOSE CONE

ORSA

ACS

T/M

EXP
ELECA

location of sep stroud
of the g-?

EXP.
VAC.
CAN
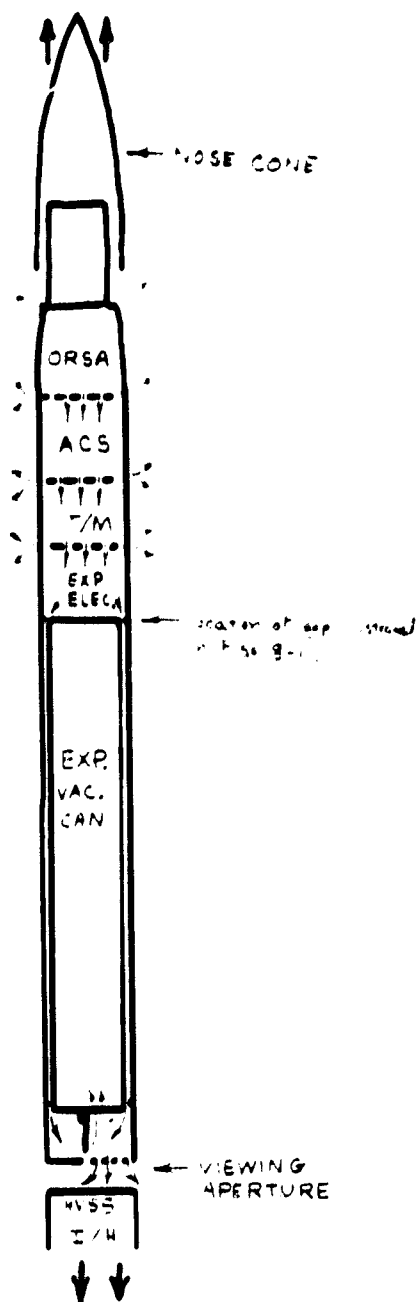
VIEWING
APERTURE

MNSS
I/H

Fig. 7

The principal restriction to the flow of air along the entire circuit is the small gap between the vacuum vessel and the skin of the payload. Figure 8 shows a detailed cross section of this gap and illustrates the route of the flow. Figures 9 and 10 show, respectively, where the thermal isolation spacers were located and the sizes of the important dimensions. If one actually computes how rapidly the 9 ft^3 volume could decompress through this annular arrangement of slots, the rate is pretty high. However, one must remember that the parachute in the ORSA will release its trapped gases at a very slow (and not easily calculable) rate.

Some additional support for the venting theory just presented might be derived from the uptick in pressure shown in Figure 6 at T = +81 sec (this was mentioned previously -- see footnote 13 on page 43). Prior to this explanation, it was hard for us to imagine how ACS gases could ever be registered by an ion gauge inside the payload, when the payload's aperture was so far removed from the thrust jets. Now, one could imagine that a small leak in the plumbing inside the ACS section could release some extra gas, which in turn would follow the other material along the aforementioned route.

To overcome the problem discussed above for the second flight of IMAPS, we implemented two fixes during the two weeks of preflight preparations at the Missile Range. First, we drilled several 1-inch diameter holes in the ACS and T/M housings and covered them with the standard streamlined shrouds. The number and diameters of these holes were judged to be adequate, by a generous margin, to insure that the chambers would pump rapidly during the ascent of the rocket. As a second precaution, we packed the slots near the thermal isolation spacers with asbestos fiber cord, so that we could be certain that the amount of air reaching the front of the payload was lower than before by *at least two* orders of magnitude (remember that the pressure on the first flight was higher than the usual pressures where high voltages break down by about a factor of 30).
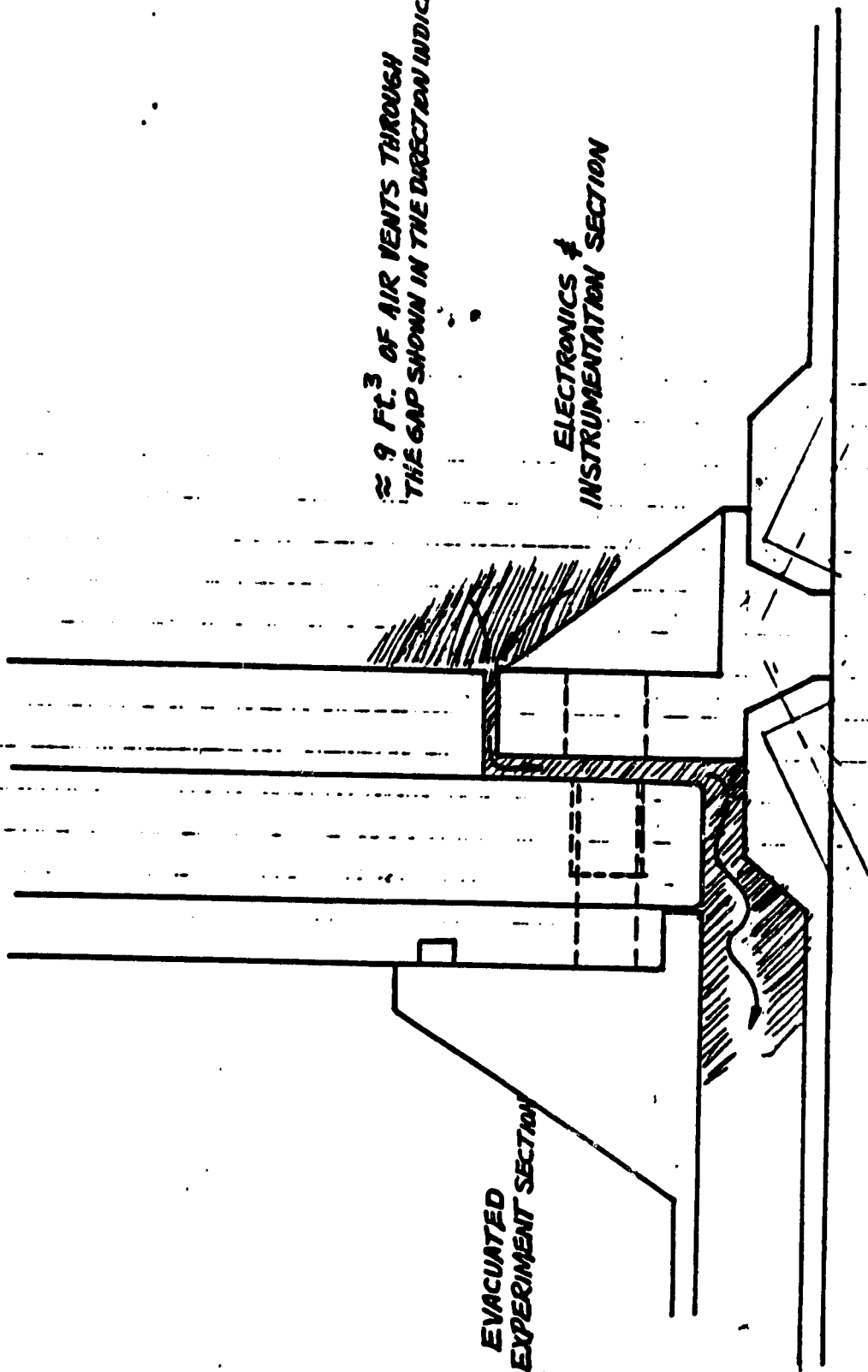
≈ 9 Ft.³ OF AIR VENTS THROUGH
THE GAP SHOWN IN THE DIRECTION INDICATED

ELECTRONICS &
INSTRUMENTATION SECTION

EVACUATED
EXPERIMENT SECTION

Fig. 8

≈ 50% OF GAP IS FILLED AS SHOWN (NEMA G-10 SPACERS).
(100% OF 0.0625 GAP FILLED ON IMAPS II FLIGHT.
(12 INCH CIRCUMFERENCE)

THERMAL SPACERS

AFT. BULKHEAD

MOUNTING RING

Fig. 9

ELECTRONICS &
INSTRUMENTATION SECTION

13.40 DIA.

0.0625

MOUNTING RING

AFT BULKHEAD

0.125
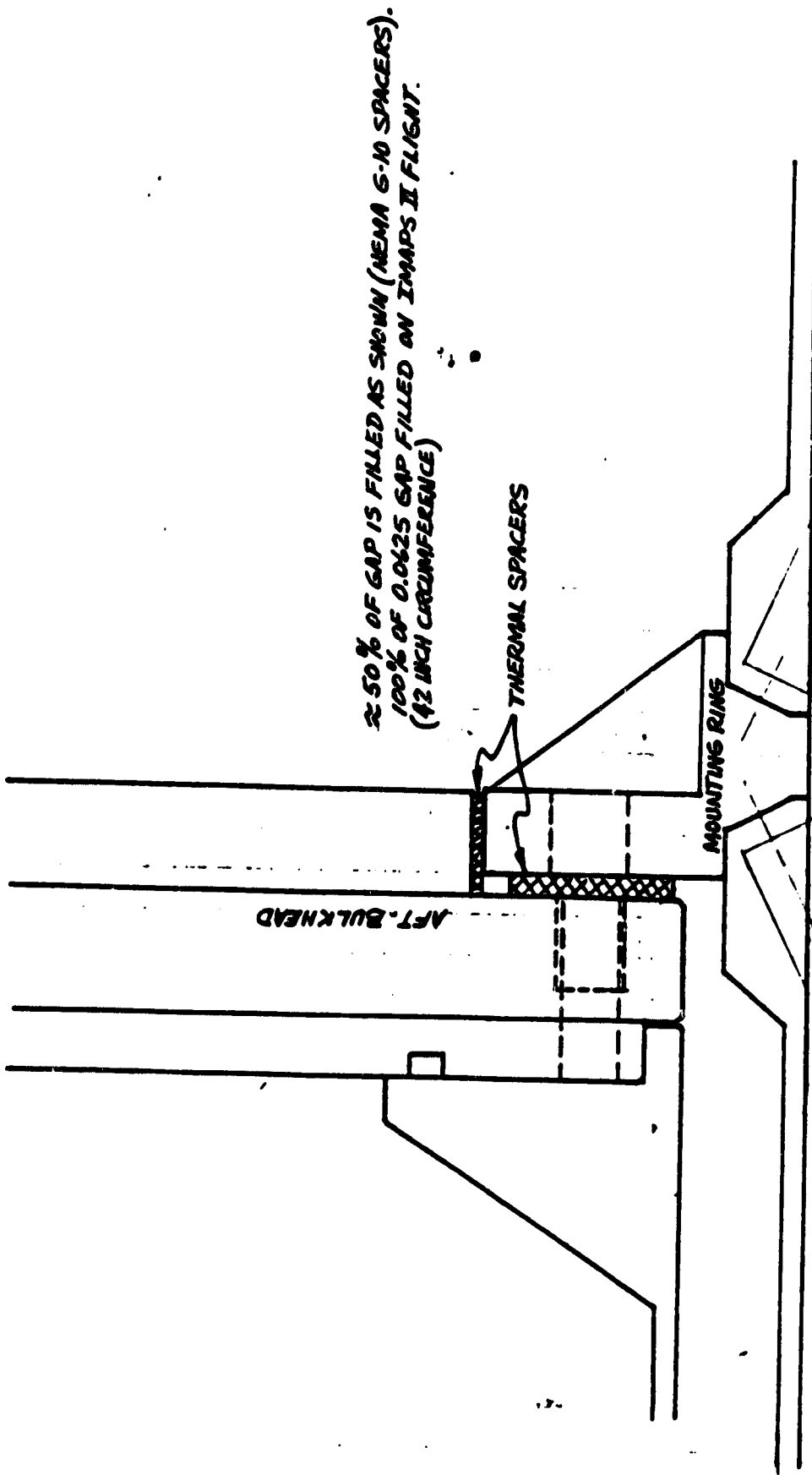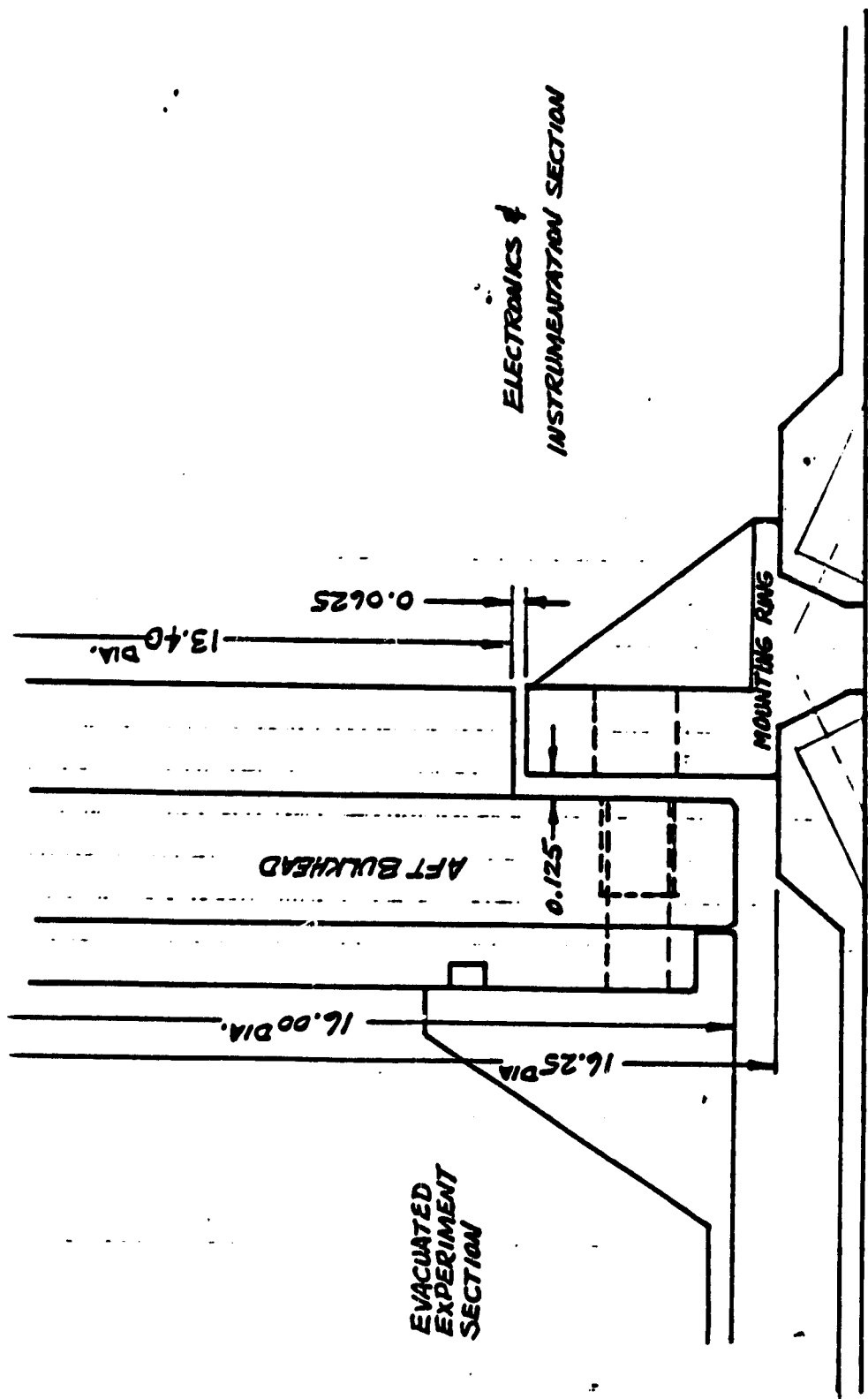
16.00 DIA.

16.25 DIA.

EVACUATED
EXPERIMENT
SECTION

IMAPS PAYLOAD 27.07 LU6 & 27.082 U6
AFT BULKHEAD & MOUNTING RING

Fig. 10

7.3. Second Flight of IMAPS on a Sounding Rocket (27.082UG)

In contrast to the first flight, the second IMAPS mission flown on April 20, 1985 (0050 MST) was a complete success, both technically and scientifically. From the real-time TV display of the detector output telemetry signal, it was immediately apparent that the payload was stabilized on target, that the detector was function- ing very well, and that a spectrum of about the right intensity was being registered. It was also clear that the Lyman-α airglow background was at about the expected level -- i.e., not strong enough to compromise the data quality.

The target on this mission was π Scorpii, a B1V+B2V type star (actually a binary system with one component very much fainter than the other) with a V magnitude of 2.88. While the interstellar spectrum toward this star is not as bizarre as that toward ε Per (see §7.2), it is still of significant interest: it has a fairly appreciable abundance of H_2 and there is a component at moderately high velocity, presumably from a shock passing through some of the gas.

At the conclusion of the flight, the payload descended into a mountainous region on the western edge of the missile range. Fortunately, it did not land on any of the nearby treacherously precipitous terrain, but the slope was moderately steep and rocky. After the initial impact on one end, the skin of the rocket and the payload's vacuum vessel were punctured by a rock as the entire assembly tipped over, landed flat, and rolled a short distance down hill. The damage was not serious, however; only minor structural members and a small part of the vessel wall were in need of repair. No internal components were broken during any phase of the flight.

At the time this report is being written, we are actively working on data reduc- tion. Sections of this report which follow give some performance data on some payload components and some of the NASA-supplied support systems (e.g., ACS, telemetry and vehicle). Some preliminary conclusions on the scientific data,

based on the limited information available at the moment, are presented in later sections.

7.3.1. Subsystem Performance and Useful Engineering Data

7.3.1.1. Rocket Vehicle Performance

According to the radar data, the payload was boosted into a trajectory which reached a peak altitude of 263.8 km at T = +265.0 sec. This altitude was slightly lower than the prediction[14] of 266.5 km, but the vehicle probably performed normally because extra weight was added to the payload. Weights were attached to the payload about a week before the flight so that the re-entry attitude would be more flat, which in turn would lead to less aerodynamic heating (on flight 27.071 the front end of the ORSA package was badly burned).

7.3.1.2. Time Profile of the Payload's Skin Temperature

A principal concern in flying the IMAPS payload is how much heat would be transferred to the skin of the vacuum vessel -- a structure which defines the distance between the only focusing element in the payload, the cross-disperser, and the detector. This wall was made of ordinary aluminum which has an expansion coefficient of of $2.6 \times 10^{-5} \, ^\circ C^{-1}$.[15] Appendix B shows calculations of the rate of temperature rise of the payload wall as it is heated by radiation from the hot rocket skin. As the last line of the calculations show, a temperature rise of about 8 °C could result over a 400 sec. interval of time, and if the spectrograph were initially at a perfect focus, the blur of the image could increase to 37μ at the end of the

---

[14]*Aeroballistic Analysis for Pre-Integration Review* by R. P. Buchanan (Code 841.1), March 19, 1985.

[15]At one time, we had considered building the optical metering structure out of graphite epoxy. We abandoned this idea because the cost was more than the program could afford at the time.

flight. It should be apparent that these calculations were rather approximate, and thus we had some concern that an out of focus condition might be worse than predicted.

Figure 11 shows the telemetered temperature data for sensors located on the vacuum vessel skin, aft bulkhead of the payload, and on the detector inside the instrument. The latter two sensors were to check that heating by the electronics was not appreciable. The skin sensor showed that the temperature increased from 23.6 °C to 33.2 °C during the time the spectral data were being recorded (+132 < T < +457 sec.). The rate of temperature rise after about T = +220 sec. was 0.026 °C s^{-1}, a figure remarkably close to the prediction of 0.020 °C s^{-1}!

In anticipation that we would be observing at elevated temperatures, the people at BASD who performed the optical alignment of the IMAPS instrument set the focus to be best at 27 °C. (Just before the flight, considerable care was made to be sure the ambient temperature for the payload was as low as we could make it, within a reasonable effort.) At the beginning of the exposure sequence, we were 3.4 °C too cold, which would theoretically mean that the focus would be wrong by 0.16 mm. With the spectrograph's f/10 beam, the blur circle would be 16μ in diameter. As the payload heated, it should have gone through perfect focus and, at the end of the data-taking sequence, would be out of focus in the other direction by 0.29 mm, because it was too hot by 6.2 °C. In short, thermal changes should have produced blurs going from about half of a 30μ CCD pixel in the beginning to the full width of a pixel at the end.

INMPS II FLIGHT TEMPERATURE
PROFILES
27.082 UG 20 APRIL 1985

VACUUM VESSEL SKIN

AFT BULKHEAD

DETECTOR

DFB 5-10-85

FIGURE II

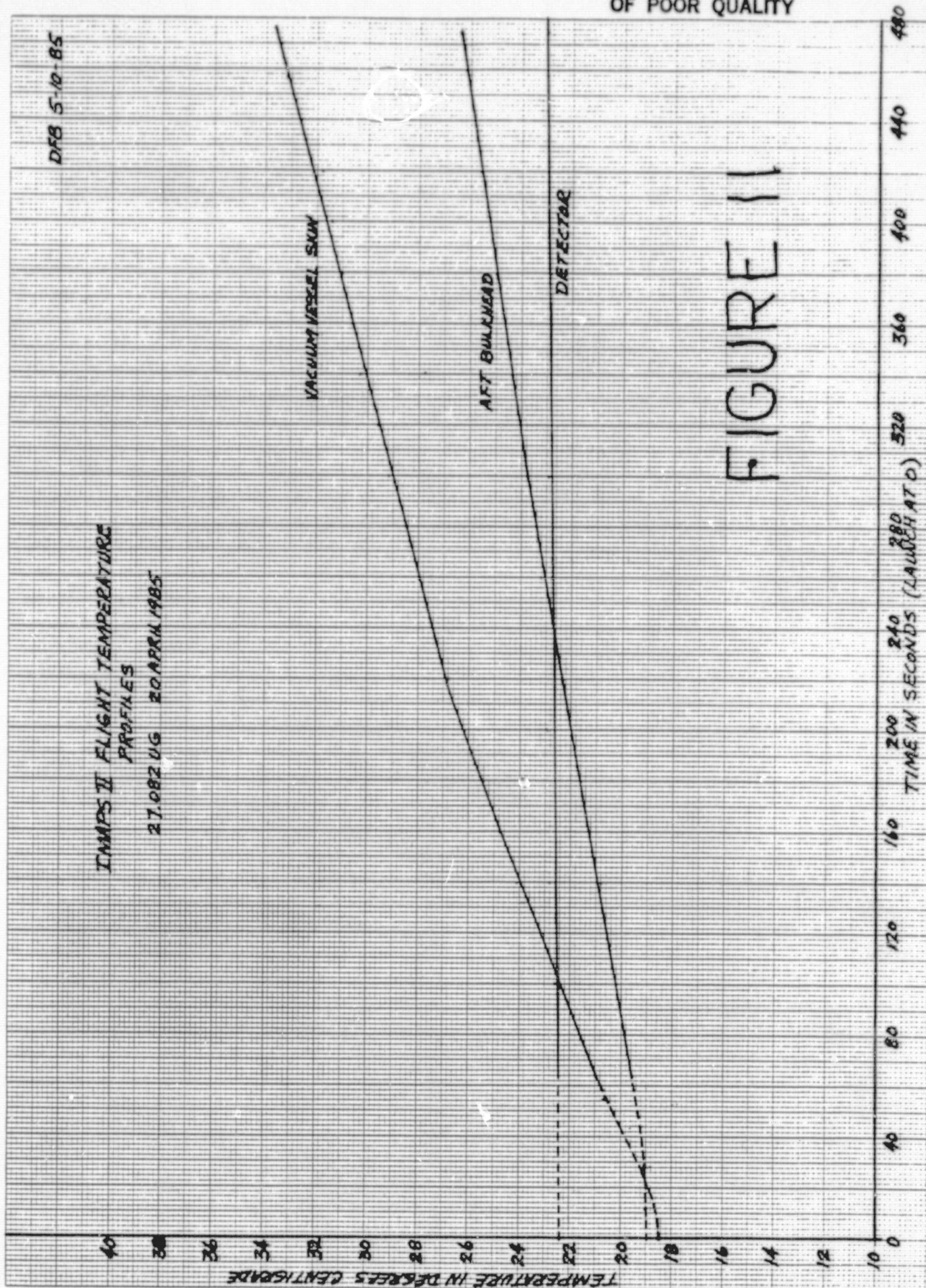TIME IN SECONDS (LAUNCH AT 0)

TEMPERATURE IN DEGREES CENTIGRADE

7.3.1.3. Attitude Control System (ACS) Performance

7.3.1.3.1. Target Acquisition

It seems reasonably certain that the ACS system pointed the payload to the correct star. ACS personnel stated that the telemetry indicated no anomalies in the maneuvers to target or in the target acquisition process. Also, the spectrum recorded by IMAPS seems, when viewed superficially, to be that which one might expect from the chosen target. However, no independent verification of correct pointing has been made by any analysis of the aspect camera pictures (the aspect camera was intended to be used only in the event that there were serious doubts about the pointing).

Figure 12 shows the stars in the field of view of the startracker. From the presence of several other stars in the general vicinity of the target which were moderately bright, the ACS group decided that there would be considerably less risk of acquiring the wrong star if an intermediate maneuver were made to the very bright star α Scorpii, so that the positions of the gyros could be updated (see§7.3.1.5).

7.3.1.3.2. Stability

The critical factor which influenced the quality of the observations was *not* the angular amplitude of the ACS limit cycle, but rather the rate of change of the pointing direction. Since IMAPS is an objective grating spectrograph, as long as the spectrum format was approximately centered on the detector and attenuation by the mechanical collimator was not significant, the absolute pointing direction could be somewhat off the target (excursions of 1 or 2 arc min could be tolerated).

FIGURE 12

FIGURE 13

X Position (parallel to dispersion)

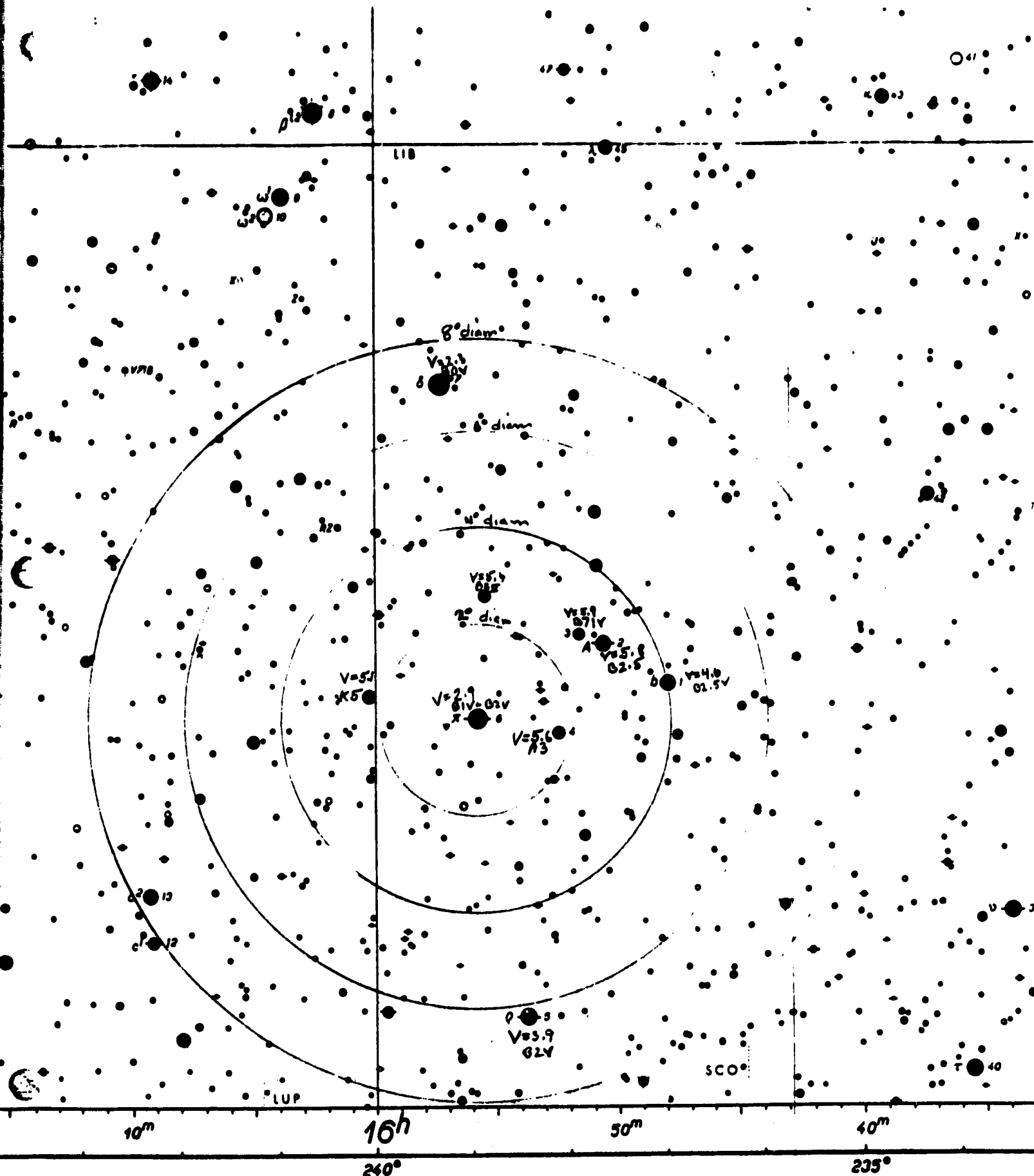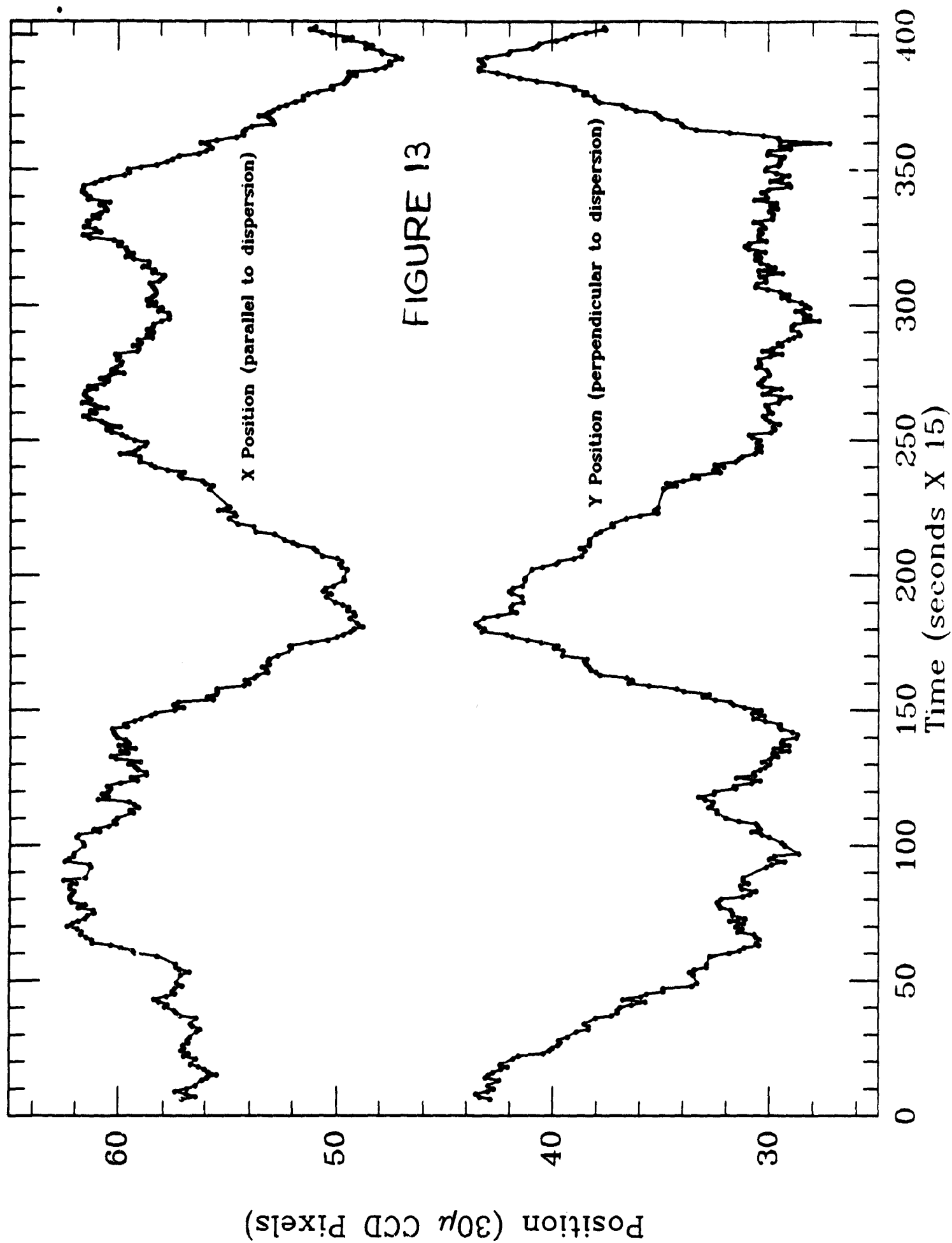Y Position (perpendicular to dispersion)

Time (seconds X 15)

Position (30μ CCD Pixels)

Small rates of change, on the other hand, were important since we must not have an appreciable smearing of the image in the 1/15 sec. frame time. In setting our requirements for ACS performance, we declared that a rate of less than 15" s^{-1} should be a specification for the ACS hold performance, while less than 5" s^{-1} should be a goal. With a rate of 15" s^{-1} the smearing would be equivalent to 0.3 CCD pixels (30μ each) per frame.

Figure 13 shows a plot of x and y positions of the broadband star image for a series of ICCD frames which have been processed up to now. Each CCD pixel corresponds to 3.45". The largest peak to peak variations are about 15 pixels (or about 52"), for the data shown here. From a visual estimate comparing the dynamic behavior of the star during this segment of time with that during the rest of the flight, it appears that the information in this plot is pretty representative of what happened during the whole data-taking session. The excursions of almost 1' may seem large by normal standards for the limit cycle for a STRAP 5 ACS system, but one must remember that we asked to trade small amplitudes for low rates, so the ACS people deliberately opened up the dead band and used low pressure bleed jets for stablization.

Each dot on the curves represents a single 1/15 second frame. Consecutive dots which are spaced by more than 0.3 pixels in the vertical direction on the plot represent cases where the 15" s^{-1} specification was violated. Figures 14 and 15 show that this happened rather frequently. Figure 14 is a histogram showing how often the displacement vector changed by a given amount from one frame to the next. These results, taken from the data shown in Figure 13, tend to overstate the excursions a bit, since some additional random walk is produced by errors in determining the centroid of the star image. (The error of this determination will add to the pointing error in quadrature, if the two effects are uncorrelated).

FIGURE 14

Total Motion $(X^2 + Y^2)^{1/2}$

FIGURE 15
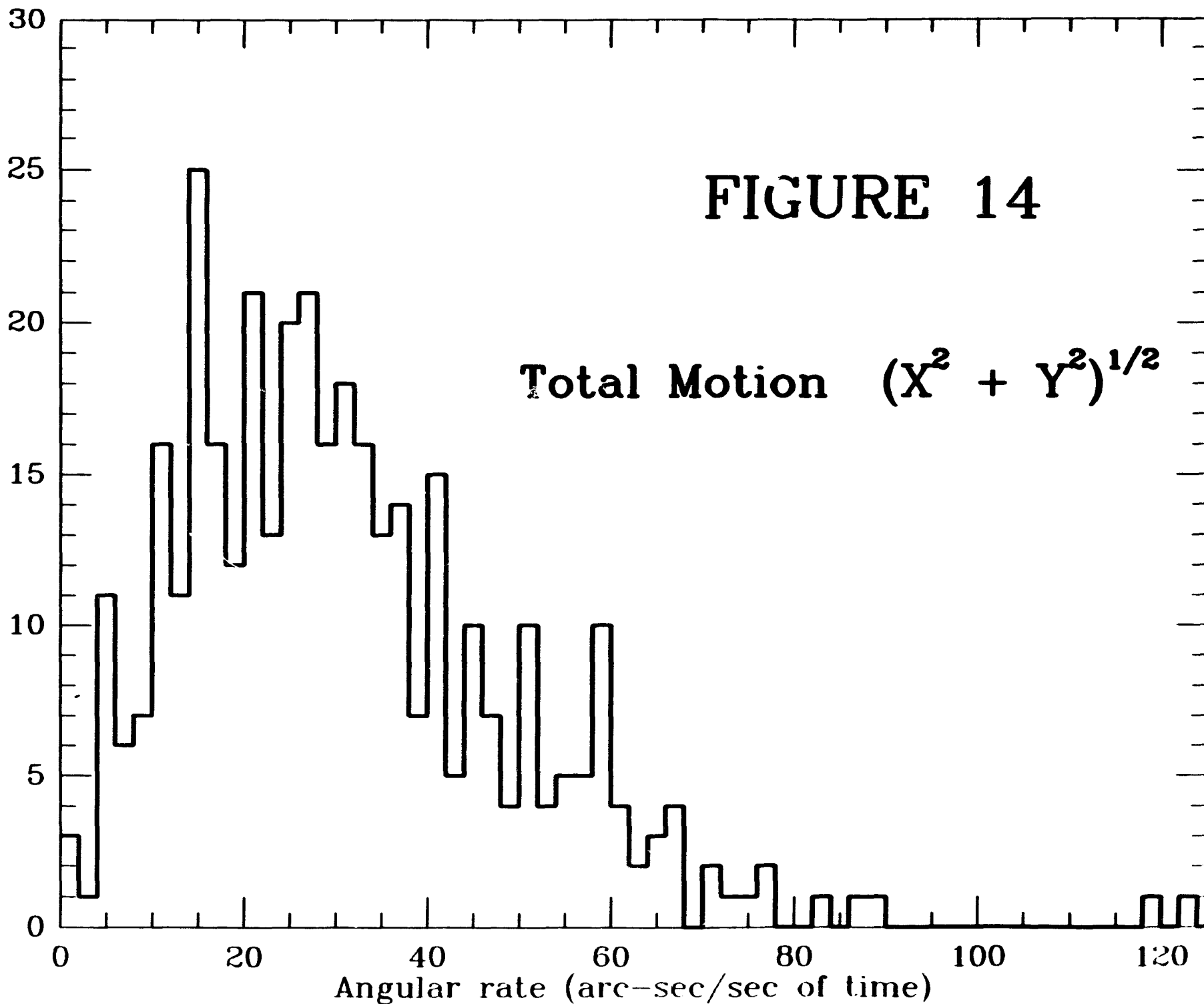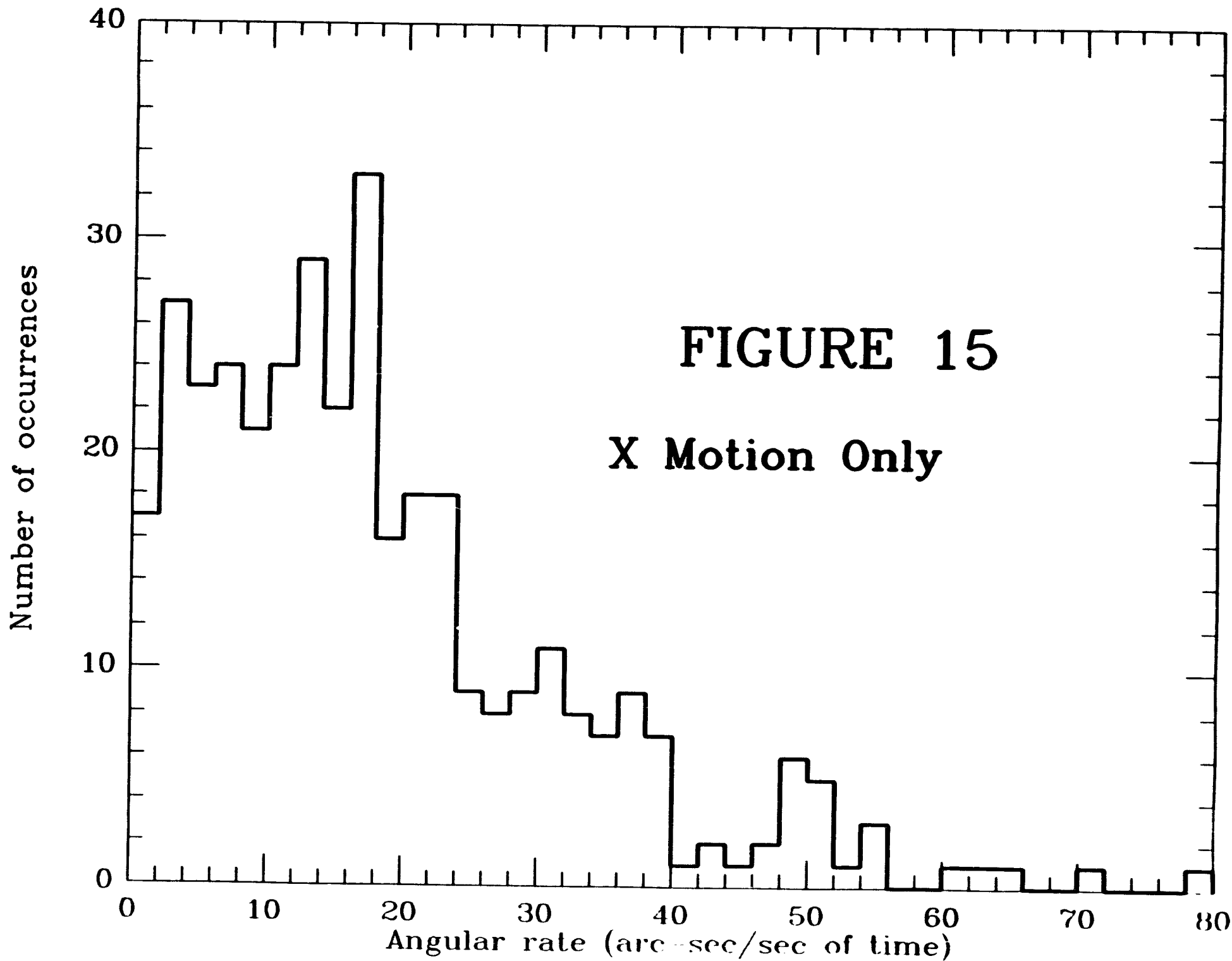
X Motion Only

The quantity which really influences the spectral resolving power of the recorded data is the smear along the X direction only (i.e. parallel to the dispersion of the echelle grating). Figure 15 shows that for a moderate fraction of the time, the rate was in excess of 25" s^{-1}, which corresponds to 1/2 pixel of smear in a given frame. When the recorded data are eventually combined to produce a spectrum for scientific interpretation, we may elect to discard those frames where the motion was relatively rapid, to recover some of the lost spectral resolution but with some sacrifice in the total number of photoevents counted (and hence signal-to-noise ratio).

7.3.1.4. Telemetry Signal Quality

A major concern early in the IMAPS program was whether or not the final signal-to-noise ratio would be adequate to register events reliably. While this requirement was absolute, we also felt that it was *highly desirable* to obtain good enough signals so that events could be centroided to an accuracy of at least half a pixel in the dispersion direction.

From preflight test results and also the outcome of the 27.082' mission, it was clear that the signal quality was fully adequate. The best signals were recorded at the Jig-67 site, as one might imagine since the diameter of the receiving dish is rather large (24 feet). Even the signals recorded at other receiving stations were adequate to meet our minimum requirement. Photoevents were clearly visible on the tape recordings derived from 10-foot dishes on the range. We were very fortunate to have at Jig-67 not only the NASA receivers with 10 MHz IFs, but we were also permitted by the military authorities to use one of their 10 MHz IF receivers. This second low-noise receiver allowed us to record both polarizations (LH and RH circular) and also have some backup capability that was as good as the primary one.

Noise measurements were performed on the VCR tape recordings of the flight telemetry, and the following results were obtained.

[1] J-67 RHC 10 MHz IF: max signal = 900 mV, 1σ noise = 5.5 mV

[2] same as [1] above except signal routed through μ-wave link to N200: max signal = 800 mV, 1σ noise = 6.5 mV

[3] J-67 LHC 10 MHz IF: max signal = 300 - 800 mV (rather ragged upper clipping level), 1σ noise = 10 mV

[4] 10-foot dish 10 MHz IF VAB/N200: Recorded on GE tape recorder (rather than Panasonic ones for [1] - [3] above). It is difficult to get the Panasonic VCR at Princeton to stabilize in the freeze-frame mode for this tape, presumably because of some sneaky incompatibility in the ways the signals were recorded. No great effort was made to measure the signal properties for this tape since we have plenty of good recordings otherwise.

7.3.1.5. Event Timing

On the two pages which follow, times and altitudes of key events during the flight are listed. This information is followed by pages which show actual times, measured off of the telemetry records, of events triggered by timers in the experiment and instrumentation sections. The exposures enumerated on the second page refer to the aspect camera in the experiment section (which ran off a timer inside the instrumentation section).

5. Specific Times/Altitudes of all Experiment Related Events

TIME (sec)	ALTITUDE (km)	FUNCTION
-600	0	Manually insert vacuum plug.
-540	0	Verify that vacuum is still good.
-480	0	Withdraw vacuum rail system.
-120	0	Verify that the rate of pressure rise within the payload vacuum enclosure is acceptably low.
-60	0	Instrumentation section removes experiment power.
0	0	Launch
40	33	Rocket burnout
60	73	Nose cone eject.
62	77	Restore experiment power; all experiment systems active except for the detector high voltage. Echelle moves from position 1 (high cam --safe for launch) to position 4.
63	79	Yo-yo Despin.
66	84	Payload separation and ACS start. Start experiment timer.
67	86	Erect pitch and yaw gyros to launch attitude and settle; eliminate residual roll using jets.
74	99	Remote adjust begin: Roll +7.13 deg. (1.47 sec) Pitch -109.86 deg. (22.76 sec) Yaw 0.00 deg. (0.00 sec) (if launch occurs at 0000 MST = 13h 47m 59s LST) for maneuver to alpha Sco (ACS update star)
96	135	Safe altitude to open experiment aperture door. (p $\sim$ 3 x 10^{-6}, in the absence of scoop effects and/or outgassing from other parts of the rocket and associated systems)
98	139	Begin settle and capture on α Sco $\alpha_{1965.5} = 16\ 28\ 31$
100	142	Open aperture door $\delta_{1965.5} = -26\ 24\ 03$
104	148	Cage gyros

10?	152	Begin maneuver to τ Sco (observing target star): Pitch -4.08 deg. (0.85 sec) Yaw +5.51 deg. (1.13 (sec)
109	156	Maneuver to τ Sco complete, begin capture and settle.
115	164	ACS hold on τ Sco for remainder of the flight.
118	168	Turn off experiment ion gauge; start detector high voltage sequencing.
120	171	First high voltage step active; continue with successively higher voltages.
130	184	Experiment detector high voltage at full level.
134	189	Change echelle tilt: pos 4 to pos 3
168	225	Change echelle tilt: pos 3 to pos 2
202	251	Change echelle tilt: pos 2 to pos 1
239	266	Change echelle tilt: pos 1 to pos 4
273	270	Change echelle tilt: pos 4 to pos 3
307	263	Change echelle tilt: pos 3 to pos 2
341	245	Change echelle tilt: pos 2 to pos 1
378	213	Change echelle tilt: pos 1 to pos 4
412	173	Change echelle tilt: pos 4 to pos 3
446	123	Change echelle tilt: pos 3 to pos 2
460	99	Close aperture door and turn off HV. Change echelle tilt to pos 1 (safe pos)
464	92	Ambient pressure reaches 10^{-3} torr --HV discharge may occur in image section, if the door weren't closed and HV turned off.
475	71	Turn off experiment power.
480	61	1st Severance and drogue parachute deployment.

NOTES:

Formula for computing approximate altitudes:

$$h(km) = [270 \text{ km} - 0.5(9.2 \times 10^{-3}) \text{km s}^{-2} (267 \text{ s} - t)^2]$$

IMAPS TIMING AT WSMR, NM

	4-10-85 PRE-HORIZ.	4-15-85 HORIZ.	4-18-85 VERT.	4-20-85 FLIGHT
T-0	0	0	0	07:49:59.651GMT
EXP.PWR.ON	61.2	62	62	63.1
SEPARATION	67	67	69	68.0
ECHELLE 1→4	90.2	100	90	97.4
APER.DOOR OPEN	101.5	102	104	101.8
HI VOLT ON	119.5	120	121.4	119.0
ECHELLE 4→3	123.5			130.4
HI VOLT FULL UP	131.2	132	133.4	132.0
ECHELLE 3→2	156.7			163.7
" 2→1	190.0			197.0
" 1→4	226.5			233.1
" 4→3	259.5			266.4
" 3→2	293.5			299.7
" 2→1	326.5			333.0
" 1→4	?62.5			369.3
" 4→3	396.2			402.6
" 3→2	429.5			436.0
HI VOLT OFF &A.DOOR CLOSE	458.5	457.8	459.0	457.0
ECHELLE 2→1	4?2.5			469.2
EXP.PWR.OFF	498.2	475.5	474.5	476.2

5-9-85
DFB

IMAPS II EXPOSURES
OTIME→07:49:59.651GMT

|			
1.	78.4 sec.	2.8 sec.	PULSE DURATION
2.	92.4 sec.	1.6 sec	" "
3.	105.5 sec.	1.6 sec.	
4.	118.4 sec.	1.6 sec.	
5.	131.4 sec.	1.6 sec.	
6.	144.0 sec.	1.6 sec.	
7.	157.8 sec.	1.6 sec.	
8.	169.3 sec.	1.6 sec.	
9.	181.8 sec.	1.6 sec.	
10.	194.5 sec.	1.6 sec.	
11.	207.1 sec.	1.6 sec.	
12.	219.5 sec.	1.6 sec.	
13.	232.1 sec.		
14.	244.3 sec.		
15.	256.8 sec.		
16.	269.3 sec.		
17.	281.7 sec.		
18.	294.0 sec.		
19.	306.5 sec.		
20.	318.8 sec.		
21.	331.2 sec.		
22.	343.4 sec.		
23.	355.8 sec.		
24.	368.2 sec.		
25.	380.6 sec.		
26.	392.9 sec.		
27.	405.4 sec.		
28.	417.9 sec.		
29.	430.3 sec.		
30.	442.7 sec.		
31.	455.1 sec.	◁──── HI VOLT OFF 456.4 sec.	
32.	467.5 sec.		
33.	479.6 sec.		
34.	493.0 sec.	LAST EXPOSURE	

7.3.1.6. Performance of the ICCD Detector

The principal characteristics and operating modes of the ICCD detector in the IMAPS instrument are presented in §6.4 of this report. §7.1 discusses in some detail the properties of the CCD which was finally selected for flight. In sections below, we cover some basic attributes of the imaging section's performance that are evident from the flight data.

7.3.1.6.1. Distribution of Event Charge Amplitudes

A program has been written which identifies discrete photoevents in areas of the image format where the event rates are low enough that there is little confusion from chance overlaps. Events are recognized by scanning for pixels which exceed a certain threshold (well above the readout noise) in frames where the CCD fixed pattern background has been removed. Once this threshold has been passed, the total charge collected in a 3×3 box centered on the hot pixel is measured. Care is taken to insure that events are not counted twice when more than one pixel exceeds the threshold in a small area. Also, events which might be contaminated by a nearby event are rejected.

Figure 16 shows the distribution of signal amplitudes which were extracted by the event detection program from a collection of frames recorded on the flight. The units given on the abscissa are arbitrary; their values correspond to the recorded voltages times a scale factor governed by a gain setting of the Colorado Video frame storage and digitization device connected to our VAX computer. The narrow bar at Relative Amplitude = 256 represents cases where signals equal to or greater than 256 were detected. These probably correspond to exactly superposed events or ion events. The tail between amplitudes 200 and 250 also probably came from superposed events that were not recognized as doubles by the program.

Figure 16
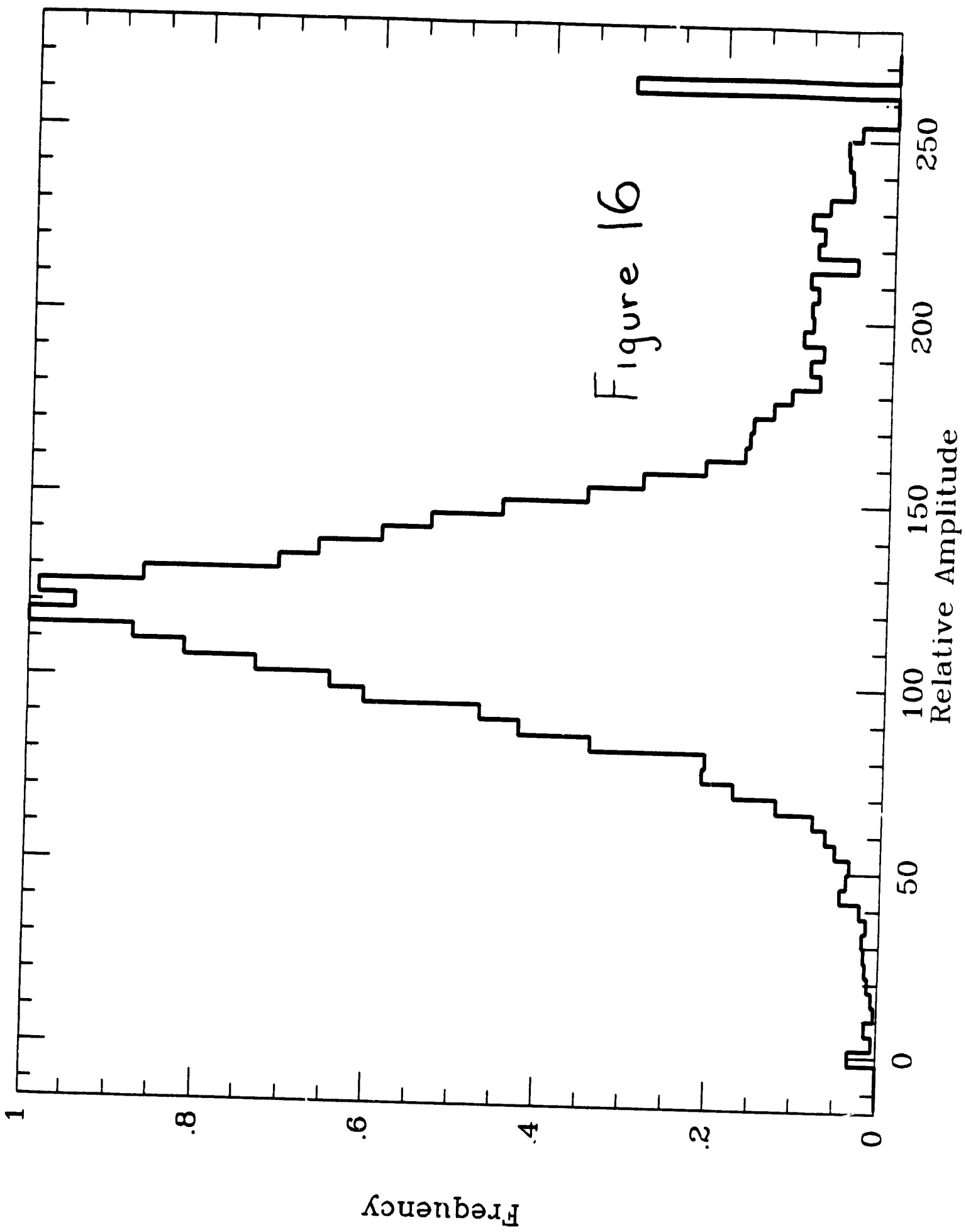
If one rejects the extended tail of the distribution at the high end by substituting in the dropoff at the low end, reflected about the distribution's axis of symmetry, one finds that the average pulse amplitude is 118.5 and the *rms* dispersion is 26.1. The peak is well separated from the random noise in the readout, which, on the scale given here, corresponds to an *rms* variation of 4.81.[16]

The ratio of the distribution function's 1σ width to its mean value is of special significance. From the numbers given above, this relative dispersion is equal to 22%. If we accumulate the recorded signal by adding the pixel intensities from frame to frame instead of counting events explicitly, the net signal-to-noise ratio should be reduced below the one governed solely by the statistical variations in counts by a factor of only $(1 + 0.22^2)^{\frac{1}{2}} = 1.024$.[17] This means that in places where the spectrum intensity is so large that the events are inseparable, an analog accumulation will have virtually the same signal-to-noise ratio as the one we would have obtained if we were actually able to identify and count the events. This is indeed fortunate, since on this flight the intensities recorded in the upper halves of the frames was great enough to require the analog coaddition of signals. We do, of course, lose our ability centroid the events (see §7.3.1.6.2 below) when they are not explicitly recognized.

---

[16]The noise in the digitized versions of the flight frames is greater than measured variations in the analog outputs discussed in §7.3.1.4. (For instance, digitized SNR = 118.5/4.81 = 24.6, while the pulses seen on the raw VCR output -- ranging from approximately 200 - 250 mV -- have a *minimum* SNR = 200/5.5 = 36.) The source of this extra noise is not understood at the moment. It may be attributable to either problems with the Colorado Video digitizer or with the VCR when it operates in the freeze frame mode.

[17]This assumes, of course, that readout noise is unimportant. A significant deterioration in signal-to-noise ratio can occur if the mean event rate is low, since the signal from each event must, on the average, compete with the combined noise from a large number of other frames containing no events in the same location.

7.3.1.6.2. Lateral Spread of Charge in Each Event

Many events have their charge registered in more than one pixel. This is caused by a lateral dispersion of the secondary charges as they migrate toward the potential wells which define the pixel boundaries. Only events which are very nearly centered on a pixel have practically all of their charge registered in one pixel. This charge spreading, if not too large or small, permits us to achieve a spatial resolving power over dimensions smaller than the 30μ pixels. Basically, one can compare the charge amplitudes in the neighboring pixels and solve for the exact position of the primary electron hit. The accuracy of the determination is governed by only 1) the signal-to-noise ratio, 2) the size of the spread function and 3) the predictability (and uniformity) of the spread function's shape.

Figure 17 shows the distribution of charge amplitudes integrated along pixel rows divided by the total charges in the respective events. Since the events hit in random locations relative to the row boundaries, an analysis of the function can yield the *average* shape of each event's actual charge distribution in the CCD. Except for some smoothing due to noise, the functional form in Figure 17 is very nearly the same as one we found much earlier in laboratory experiments using CCDs in slow-scan readout.[18] The earlier study indicated that the charge spread behaved in one dimension as an exponential with a scale length of 0.135 pixels. This size for the distribution is very nearly ideal for attaining an accurate solution for the event centroid, with a given signal-to-noise ratio. As an example, if the readout noise in a single pixel is 1/20 the total charge of an average event, we calculate the *rms* error in position along one dimension ranges from 0.013 to 0.426 times the length of a pixel, depending on whether the hit occurred near a pixel

---

[18]When a CCD is read out slowly (for instance, one frame every 10 seconds instead of the 1/15 second frame period for IMAPS), one can achieve a better signal-to-noise ratio. However the CCD must be cooled, to keep the accumulation of dark current at a reasonable level over the relatively long integration time.

boundary or in the center of a pixel, respectively.

7.3.1.6.3. General Appearance of a Frame

Figure 18 shows a single frame recorded on the flight. The echelle orders are barely perceptible as linear groupings of events stretching horizontally. At the bottom of the picture is the very bright image of the star formed by one of the mirrors described in §6.6. The motion of this spot from frame to frame was used to obtain the ACS pointing information described in §7.3.1.3.2. As mentioned in the previous paragraph, the top half of the format is very busy with events and will need to be analyzed by analog coadding of pixel amplitudes. Event recognition can be accomplished for the much weaker part of the spectrum in the lower half. The picture is divided into 16 panels because there were interruptions which occurred during the standard TV broadcast line and vertical retrace intervals (see §6.5).

Figure 19 shows a magnified portion of the panel which contains the broad-band star image. In this presentation one can clearly see the intensities registered for the individual pixels. It is possible to see examples of the charge sharing between adjacent pixels responding to a single event, as discussed in §7.3.1.6.2 above. The thin, rectangular block of pixels which appear to be anomalous in the upper right portion of the picture do not contain valid image information; these pixels were overwritten by the character insertion generator which was used to identify the precise time each frame was recorded. Blocks of this type can be seen in each of the panels displayed in Figure 18 (the character information is scrambled when the broadcast TV image's interlaced lines are rearranged for the IMAPS detector display -- portions of the unscrambled numbers are written on the right hand edge of the picture).
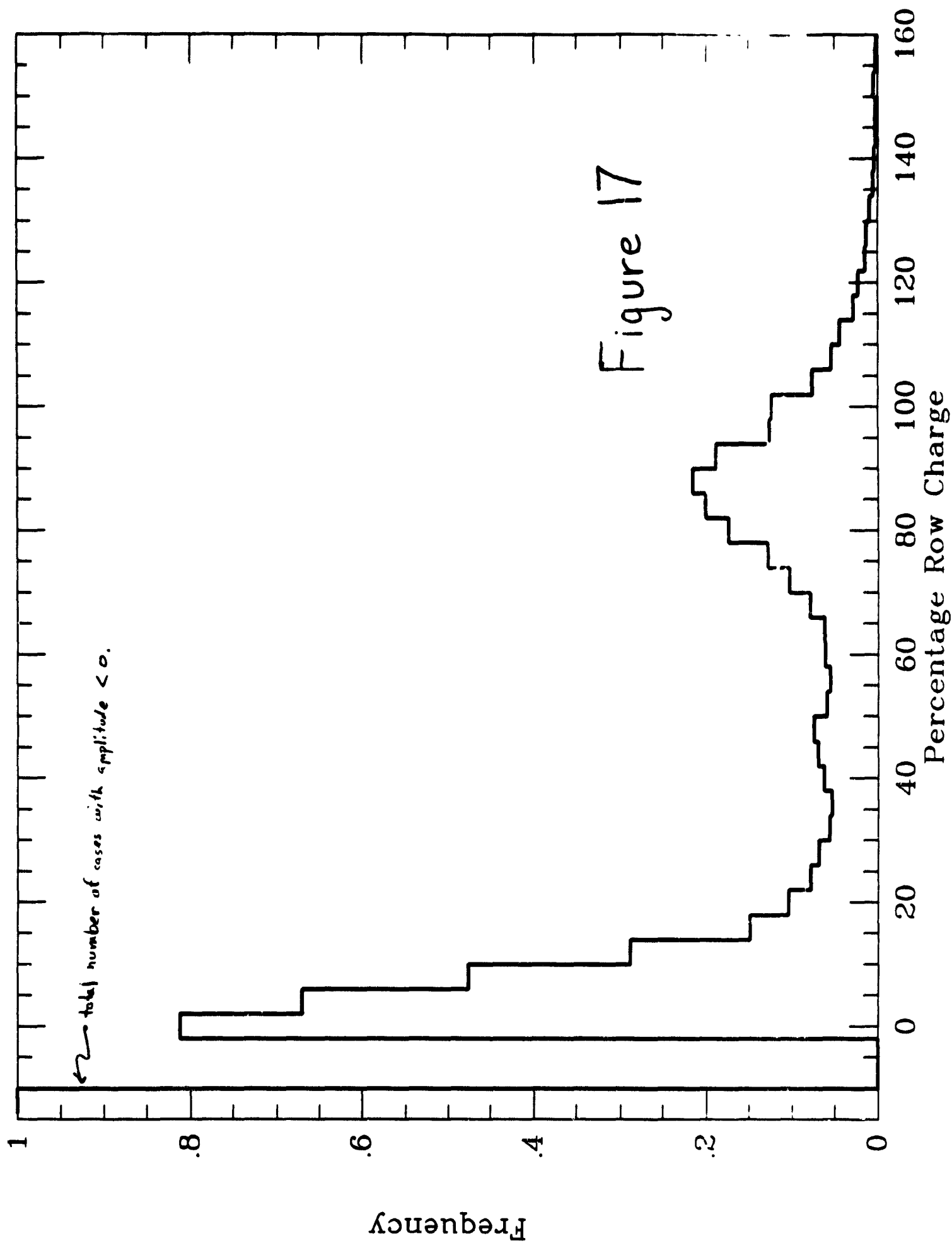
Figure 17

Percentage Row Charge

Frequency

total number of cases with amplitude < 0.
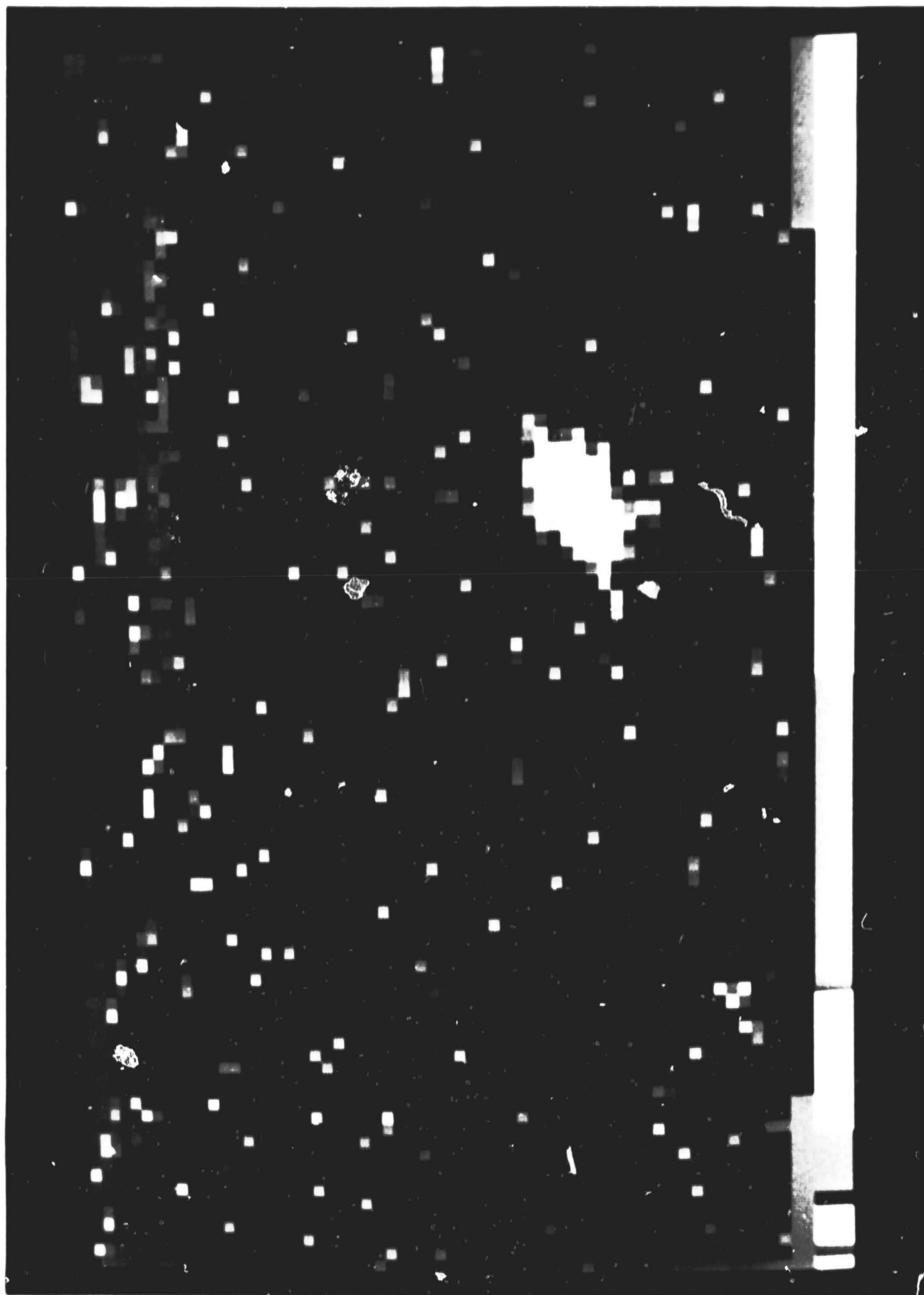
7.3.1.6.4. Rate of Ion Events

For 70 frames which were recorded at an altitude of 270 km (very near apogee), there appeared to be a total of 73 ion events. The actual number of events may be lower than this number because some of the spikes with large amplitudes may have been multiple (legitimate) photoelectrons. The 73 hits in 70 frames translates to an event rate of 1.9×10^{-4} hits pix^{-1} s^{-1}.

7.3.1.7. Sensitivity of the Entire Instrument

A measurement of the continuum of π Sco between 1141.00 and 1141.20Å gave an average count rate of 0.75 count pix^{-1} frame^{-} This level refers to the intensity above a background composed of scattered light plus the diffuse Lα background (see §7.3.1.8 below). We estimated the true flux from π Sco within this wavelength interval by two methods: 1) The low-resolution (U2) *Copernicus* scans of this star reported by Snow and Jenkins[19], using an average of the counts recorded at the two end-point wavelengths and their reported sensitivity of the *Copernicus* spectrometer at the time, and 2) *IUE* absolute fluxes near 1140Å for the V = 6.15 magnitude B1V star HD31726.[20] The IUE intensity of 7.5×10^{-10} erg cm^{-2} s^{-1} Å^{-1} (= 42.8 phot cm^{-2} s^{-1} Å^{-1}) was multiplied by a factor of $10^{0.4(6.15 - 2.90)}$ to account for the differences in visual magnitudes and $10^{-0.4(0.03)(8.1)}$ to correct for the fact that π Sco has $E_{B-V} = 0.08$ while that for HD31726 is only 0.05. (The factor 8.1 is the average value of $A_{1140Å-V}/E_{B-V}$ reported by Savage and Mathis[21].) The *Copernicus* and *IUE* values of 580 and 680 phot cm^{-2} s^{-1} Å^{-1}, respectively, were averaged to obtain a flux of 630 phot cm^{-2} s^{-1} Å^{-1} from π Sco. Since each 30μ pixel on the CCD

[19]Snow, T. P. and Jenkins, E. B. 1977, *Astrophysical Journal Supplement*, 33, 269.
[20]*IUE Ultraviolet Spectral Atlas*, International Ultraviolet Explorer (IUE) NASA Newsletter no. 22 (Special Edition), p. 74.
[21]Savage, B. D. and Mathis J. S. 1979, *Annual Reviews of Astronomy and Astrophysics*, 17, 73.

subtends 0.00475Å at 1140Å, we find that the effective area of IMAPS (i.e., the product of the geometrical aperture area, instrument's optical efficiency and the detector's quantum efficiency) is 3.76 cm . This value is 2.5 times a lower limit for the efficiency we measured at NRL before the flight[22], but only 0.61 times the figure of 6.14 cm^2 we calculated for the product of measured and expected efficiencies of the components in the instrument (249 cm^2 aperture × 0.74 unobscured portion of the beam through the collimator × 0.83 ratio of the principal [zero order] beam to the collimator's total throughput, including diffraction spikes × 0.25 efficiency measured for the echelle grating[23] × 0.24 efficiency measured for the cross-disperser grating[23] × 0.67 quantum efficiency usually obtained at this wavelength for a KBr photocathode on a solid substrate).

We suspect that the most probable reason for the actual efficiency being somewhat lower than expected was that the photocathode degraded slightly. In spite of our using our best efforts to keep the KBr away from any humidity during the installation of the photocathode, we think some exposure to slightly humid air may have occurred. At one point, the payload had to be opened to repair a suspicious connection on a plug associated with the detector electronics. This field repair was done at WSMR long after the photocathode was installed. It is also possible that the reflectivities of the gratings could have deteriorated slightly. Finally, it seems to be generally true that astronomers discover that an assembled instrument has an overall efficiency which seems to be noticeably lower than the product of the efficiency of the separate components, for reasons they seem never

---

[22]When we exposed the IMAPS payload to a collimated beam from an argon discharge source, we found the effective area to be 1.5 cm^2. We knew at the time that this measurement was a lower limit for the sensitivity of IMAPS at 1048 and 1067Å because 1) The comparison monitor (a calibrated channeltron detector) also registered Lα and various emission lines from other impurities in the source, and 2) A significant percentage of the hits which were evident on the IMAPS frame were probably double events (they showed up with approximately twice the normal amplitude).

[23]See Appendix C: notes recorded by D. Windt (U. Colorado) when he measured the efficiencies of our gratings.

able to explain satisfactorily.

7.3.1.8. Background Light

7.3.1.8.1. Diffuse Lα Background

In the lower left panel of each frame, we recorded an average of 40 counts frame^{-1}.[24] Since the sample area of this panel is 65×60 pixels, we must have recorded 0.155 events pix^{-1} s^{-1}. The bottom of the frame is about 0.33° away from the point where on-axis Lα light would be imaged; some baffling by the mechanical collimator (see Fig. 4) makes this rate about 33% lower than the maximum rate, i.e., that which would be seen just beyond the top of the frame. For a background of 2 kR (2×10^9 phot/4π str), the Lα intensity we would have expected for a flight occurring near local midnight, we calculated beforehand that the rate should have been 0.244 events pix^{-1} s^{-1}. This value was derived from the component efficiencies listed in parentheses in §7.3.1.7 above, except for a deletion of the 0.83 diffraction factor for the mechanical collimator and a substitution of 0.50 for the quantum efficiency of KBr at 1216Å. The fact that our instrument was about 61% as efficient as predicted (at 1140Å) suggests that we really should see 0.15 counts pix^{-1} s^{-1} for a background of 2 kR. Our prediction that we would be exposed to 2 kR of Lα glow seems, in retrospect, to have been not too far from reality: the inferred value from the above arguments is (0.155/0.150)×(1 - 0.33)$^{-1}$ × 2 kR = 3.1 kR.

---

[24]Some of these counts may have come from the very weak spectrum, but it is not likely that this contribution is significant.

7.3.1.8.2. Scattered Light from the Gratings

At the bottom of a strongly saturated absorption feature (N I absorption at 1134.415Å) we measured a background of 0.17 counts pix^{-1} $frame^{-1}$. After subtracting the contribution from the La glow, the scattered light flux is 0.15 counts pix^{-1} $frame^{-1}$, which is about 28% as large as the *local* continuum on either side of the feature.

Presently, it is not possible to say how much of the contribution of grating scatter comes from small angle deflections by the echelle along its dispersion direction, or alternatively, how much of it is derived from much larger angle scatter from either the echelle or cross-disperser grating. One way to disentangle these two effects may be to learn whether the levels at the bottoms of the strong absorption features are correlated with the immediately adjacent continuum or with more global intensities of the spectrum.

7.3.1.9. Spectral Resolution

Initially, we were concerned that the instrument was slightly out of focus because the orders were relatively fat — about 2 to 3 pixels wide at any instant. However a sharp component in one of the spectr n lines seen in preliminary stacked data presented in the next section (§7.3.2) seems to show that *a lower limit* for the resolving power is about 2 pixels (FWHM), which corresponds to 2.5 $km\ s^{-1}$ in radial velocity. Since actual absorption features from gases in the interstellar medium may already have some natural broadening due to a dispersion in velocities, one could suppose that the instrumental resolution could be even somewhat better. On the other hand, one must be very careful not to draw premature, overly optimistic conclusions by selecting the sharpest looking line from a large collection of examples, since noise fluctuations undoubtedly make *some* line appear sharper than they really are. A more definitive assessment of the spectral

resolution will need to be made after more frames have been stacked (to reduce the effects of noise) and more careful compensations for star motion have been implemented.[25]

From the fact that the spectrum lines seem to be narrower than the order widths, one is left to conclude that the image must have had some astigmatism. The image points were pi obably elongated vertically (perpendicular to the echelle dispersion direction) but still rather narrow in the horizontal direction which really mattered for high spectral resolving power. The vertical elongation was probably a fortunate accident, inasmuch as it reduced the pileup of photoevents in individual frames.

7.3.2. General Character of the Scientific Data

Presently, only a very small fraction of the frames recorded on flight 27.082UG have been reduced. However, from a glimpse of the data on hand at the moment we can predict the character of the spectra which will ultimately be produced.

The entire free spectral range of the echelle was covered by the four discrete echelle tilt settings for which data were recorded sequentially (see pages 69 and 70). Positions 1 and 2 were near the peak of the echelle blaze. Hence, exposures taken at these two tilt angles showest the most intense spectra. Positions 3 and 4 show much fainter spectra because the angles of incidence and diffraction were somewhat removed from the optimum angle.

---

[25]So far, corrections for pointing offsets use the instantaneous computations for star image centroids of the type shown in Figure 13. Judging from the fine-scale jitter in the plotted points, one might suppose that each determination has a an error of about 1/2 pixel. Thus, some improvement in the offset calculation might result by replacing the scraggly curves with best fitting straight line segments bridging between the times when the ACS valves were known to have fired. Also, better registration of the stacked events might be achieved after an investigation of possible distortions of the image mapping. Some groups of stacked data with large excursions of the star position seem to show a small offset, after the normal correction procedure which assumes that the spectrum moves in exactly the same manner as the star image. Finally, better resolution might be achieved if we discard frames taken when the movement was too fast -- see §7.3.1.3.2.

Figure 20 shows an image taken at echelle position 2. This picture was created by stacking the pixel amplitudes from 390 frames (i.e., 26 seconds worth of exposure time) with the position compensations to freeze the star image at the bottom in one position. (The star image is black in the center due to integer overflows in the computer.) Echelle orders at the top of the picture are at about 1170Å, while extremely faint ones at the very bottom correspond to 958Å. Most of the prominent absorption lines are from molecular hydrogen in the interstellar medium. The missing order about 2 inches from the bottom of the picture occurs near 1025Å, where there is very strong absorption by the Lβ line.

Figure 21 shows the right-hand part of the spectrum extracted along order 206, which is the 14th order from the top in Figure 20.[26] Each dot in the picture represents the intensity recorded in a single CCD pixel, hence the separation between dots corresponds to a doppler shift of 1.25 km s^{-1}. Assuming the principal contribution to the noise is from counting statistics for the photoevents (see the discussion in §**7.3.1.6.1**), the 1σ uncertainty in each point should be 5.2 intensity units.

It is interesting to compare the preliminary reduction of IMAPS data taken over a brief time interval with scans of the very same spectrum lines recorded for π Sco by the high-resolution scanner (U1) in the spectrometer of the *Copernicus* satellite. Figure 22 shows the *Copernicus* data. Here, the signal-to-noise ratio is vastly superior to that shown in Figure 21, but the detail in the profile structure, particularly that of the Fe II absorption, is almost entirely lost, owing to the much lower resolution.

In the echelle setting shown here (position number 2), we have approximately 88 seconds worth of exposure time. Hence, we should ultimately see an

---

[26]The plot in Figure 21 was taken from a stack of 356 frames, rather than the 390 frames represented in Figure 20.
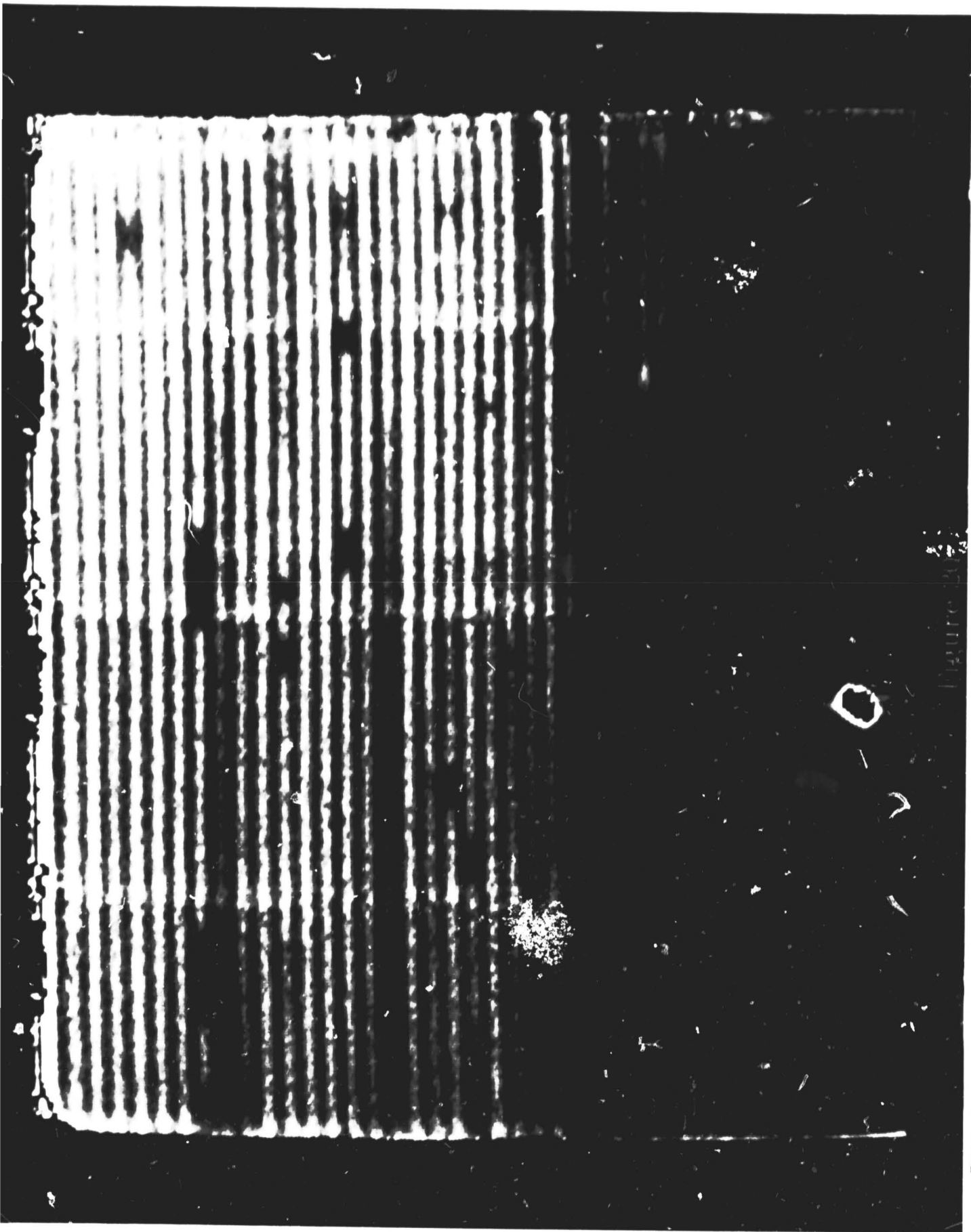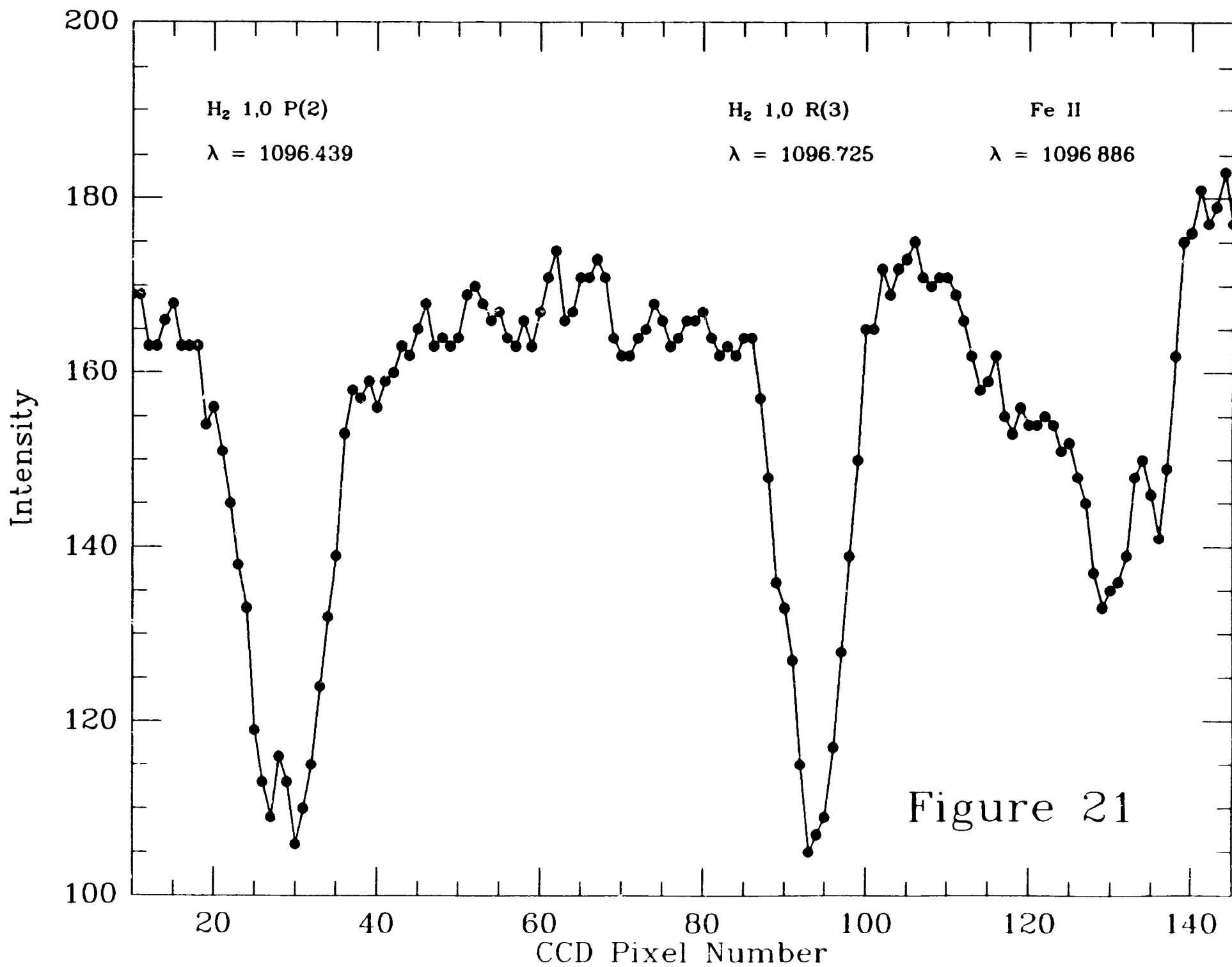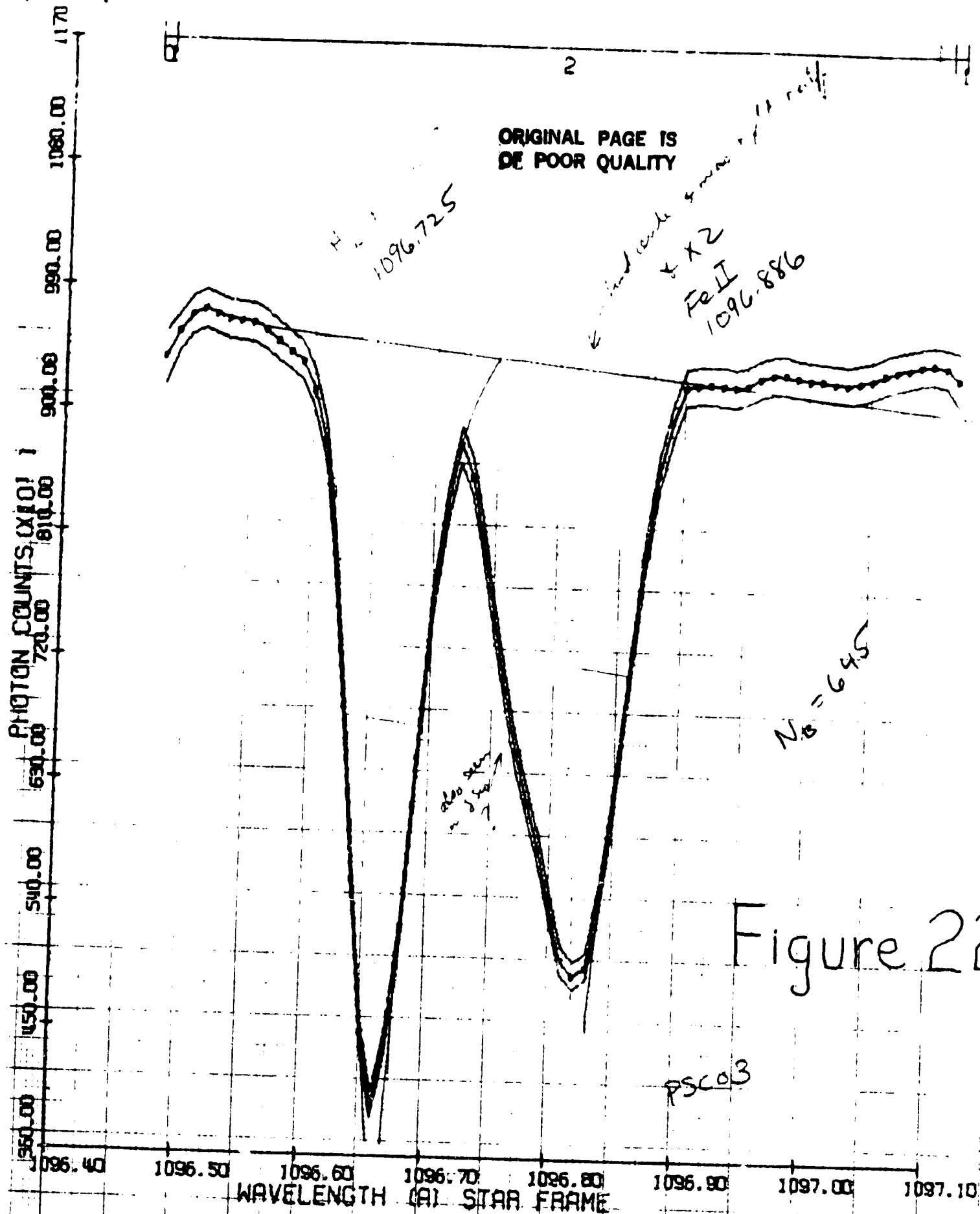
Figure 21

Figure 22

improvement in the signal-to-noise ratio by a factor $(88/24)^{\frac{1}{2}} = 1\,9$. For other echelle positions which covered the remaining quarters of the free spectral range we had the following integration times: Position 1 = 72 s, Position 3 = 98 s, and Position 4 = 67 s.

8. FINANCIAL STATUS OF THE PROJECT

Total Award .... $ 1,243,281

Expenditures

Princeton .... $ 211,905

Subcontract: BASD .. .. $ 1,031,376*

$ 1,243,281

Balance, 6/30/85 .... $ 0

> *This figure represents the full amount of the subcontract with Ball Aerospace
> Systems Division (BASD) and is subject to adjustment pending receipt of a final
> invoice reflecting final burden rates through 1983 and final fee payment.

9. KEY PERSONNEL ON THE PROJECT

Princeton University

Principal Investigator	Edward B Jenkins
Engineers	John L. Lowrance (technical director) Paul M. Zucchino (ICCD electronics design) Donald C. Long (ICCD electronics design) Michael Reale (ICCD electronics design)
Technicians	John Opperman, Jr. (vacuum system) William G Harter (electronics)
Student	Eric M. Wilcots (data digitizing)
Administrative Officer	Donald B. Hortenbach

Naval Research Laboratory

Co-investigator	George R. Carruthers

Ball Aerospace Systems Division (BASD)

Engineers	Dan W. Simmons (program management) Donald F. Bradshaw (program management) Murk Bottema (optical design) W. Alan Delamere (ICCD image section design) Richard P. Wooley (ICCD magnet design) Roger A. Misch (Electronics design) Gerry A. Seigal (Production) Arthur A. Olson (optical alignment) Georg H Becker (optical alignment) Gary P. Emmerson (optical alignment)
Technicians	Davell L. Armstrong (electronics) Max G. Hedges (electronics) John J. Kersbergen (GSE & HVPS) David E. Warlick (mechanical) Reginal L. Eckhard (machinist)

APPENDIX A

Selection of BASD for the IMAPS Subcontracting Effort

The attached letter dated June 2, 1978 was sent to six firms judged at the time to be capable of supporting the payload's design, fabrication, and field operations. We elected to engage a company prior to the preparation of a proposal to NASA, so that we could draw upon that company's resources and expertise in defining the technical aspects of the payload design. The conditions of our request for proposals are clear from the contents of the letter.

The response to our letter was as follows:

Ball Aerospace Systems Division (BASD)
Boulder, Colorado

Perkin-Elmer Corporation
Norwalk, Connecticut

American Science and Engineering, Inc.
Cambridge, Massachusetts

} proposals submitted

Itek Corporation
Lexington, Massachusetts

indicated that they were too busy to support us

General Electric Company
Philadelphia, Pennsylvania

Westinghouse Systems Development Division
Baltimore, Maryland

} no response

The three proposals we received were reviewed by four people at Princeton, working independently. To have a uniform system for judging the proposals, we agreed to score each of the 7 items (excluding item 4) listed on page 2 of the letter, and derive a grand total score by summing with the following weight factors:

item number	weight
1	1.0
2	0.7
3	1.0
5	1.0
6	0.4
7	1.0

Each of the four evaluations gave the greatest grand score to BASD. In view
of the fact that these independent decisions were unanimous, we felt there
was no need to hold a formal conference to discuss the issues before we
announced a final decision.

June 2, 1978

List of Companies to whom the contract letters for (AO) were sent.

Mr. G. J. Chodil
Technical Tower, 5th floor
Ball Brothers
Box 1062
Boulder, Colorado   80306

Mr. John Russo
Perkin-Elmer Corporation
50 Danbury Road
Norwalk, Connecticut 06856

Mr. David Ellenbogen
Vice President of Marketing
American Science and Engineering, Inc.
955 Massachusetts Avenue
Cambridge, Massachusetts 02139

Mr. Fred Gilligan
Itek Corporation
10 Maguire Road
Lexington, Massachusetts 02173

Mr. Tom Sherlock
Room U-3225
General Electric Company
P.O. Box 8555
Philadelphia, Pa. 19101

Mr. Fred Schaff
Westinghouse, Systems Development Division
P.O. Box 746 - Mail Stop 431
Baltimore, Maryland 21203

DEPARTMENT OF ASTROPHYSICAL SCIENCES

PEYTON HALL

PRINCETON, NEW JERSEY 08540

June 2, 1978

In response to a forthcoming Announcement of Opportunity (AO) for Space-
lab payloads, Princeton University Observatory is planning to submit a proposal
to fly an echelle spectrograph for observing high-resolution spectra of bright
stars in the range 900-1200 $\mathring{A}$. We anticipate that this AO will be for Spacelab
Flight No. 3 and an indefinite number of subsequent flights; the review and
acceptance of proposals will be on a periodic basis. While the release date
for the AO is uncertain, we expect that it could be issued as early as June 15,
and we anticipate that our proposal would be due about 90 days later, if we were
to meet the deadline for an initial selection of flight programs. We expect that
NASA will announce its choice of winning proposals from the first review in early
1979.

The proposed instrument will consist of a mechanical collimator, objective
echelle grating, cross dispersion grating, focusing mirror, and a windowless
image tube for data acquisition. To achieve a desired resolution of $\lambda/\Delta\lambda = 10^5$,
we plan to use an echelle with a high blaze angle -one possibility is a Bausch
and Lomb 8" x 16" grating with 79 lines mm^{-1} and a 63° blaze. The mechanical
collimator will exclude light from undesired stars and the Lyman-α diffuse back-
ground. We currently have a mechanical collimator which we can salvage from a
similar echelle spectrograph payload which was flown on an Aerobee rocket.

In addition to proposing for Spacelab, Princeton is considering the possi-
bility of flying this payload on small sounding rockets. These flights would
occur well before the Spacelab mission and would yield valuable scientific data,
as well as give us a head-start in the manufacture and space qualification of
the hardware. For the immediate future, however, our energy will primarily be
directed toward responding to the Spacelab AO. With minor modifications, this
same proposal could be submitted for consideration as a potential rocket instru-
ment.

Princeton wishes to assemble a proposal team, including an industrial firm,
prior to or nearly coincident with the release of the AO. The selected industrial
firm would assist Princeton in preparation of the proposal to NASA, supporting
their proposal effort with their own funds. It would be Princeton's intention,

in the event of the contract award, to subcontract to the same industrial firm for the majo effort involved in providing the instrument for flight. It is envisaged that Princeton will supply the imaging detector, since Princeton has already developed such devices for other programs.

Since the plan outlined above excluded a competitive selection of a contractor to Princeton after award of the NASA contract, we plan to select the industrial team member via proposals submitted by interested industrial firms. These proposals are not expected to be a facsimile of the proposal to NASA. They will not address the technical details in any depth but will be relatively brief proposals covering the following areas:

1. Name and experience of Program Manager and other key people, with their areas of technical responsibility, who would be assigned to the effort.

2. Proposed organization of the program and total magnitude of effort in man-months that the corporation is willing to devote to the preparation of a joint proposal.

3. Expected continuity of personnel from the design and proposal writing phase to the execution of the subcontract in the event NASA approves the building of a flight instrument.

4. Name, title and address of the corporate officer responsible for this work.

5. Brief description of other relevant programs recently carried out by this division, including cost and schedule performance.

6. Facilities available for fabrication and test of equipment.

7. Present overhead rate, G&A, and fees for recent comparable programs.

Firms which responded to Princeton's request in late 1976 to propose for supporting the Wide-Field Camera on the Space Telescope need not cover Items 5, 6, and 7 above if they wish not to supplement or modify this information. It is Princeton's intention to include in the subcontract for the work a condition that any change in Program Manager will be made only with Princeton's consent.

While we are not planning to hold a formal pre-proposal briefing on the programmatic or technical details of the effort, we welcome inquiries or visits from those firms which have a serious interest in supporting our program. Any commitments made in your proposal will be contingent, of course, on whether or not NASA actually issues the AO; while such distribution is expected, it is not assured. Proposals must be received no later than June 20, 1978 to be considered for selection.

Inquiries should be directed to John L. Lowrance. Telephone: (609) 452-3805 (or 3803).

Very truly yours,

Edward B. Jenkins

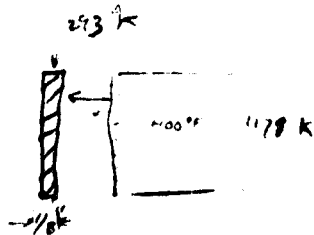EBJ/.m

APPENDIX B

Calculation of Temperature Rise

Specific heat of Al = 0.226 gm-cal g^{-1} $°C^{-1}$ = $9.45E6$ $ergs/g/°C$; coef of expansion 2.57×10^{-6}

$\sigma = 5.7 \times 10^{-5}$ erg cm^{-2} $°K^{-4}$ s^{-1}

ρ_{al} = 2.7 g cm^{-3}

$\frac{1}{8}$ slab of al = $0.125(2.54)$ 2.7 g cm^{-3} = 0.85 g cm^{-2}

293 $°K$

(Ignore cylindrical geometry)

$\sim 400°F$ $478 °K$

$-478 °K$

Emissivity of al not very certain; here are possibilities:

al   unoxidized : 0.028 @ $100°C$ oxidized : 0.11 @ $200°C$

0.060 @ $500°C$ 0.19 @ $600°C$

Let's assume oxidized case, then ϵ_{293} = 0.13 and ϵ_{478} = 0.16

High temperature radiation :

$\epsilon\sigma T^4$

$\epsilon\sigma T^4$

$(1-\epsilon)\epsilon\sigma T^4$

$(1-\epsilon)^2\epsilon^2\sigma T^4$

$(1-\epsilon)^2\epsilon\sigma T^4$

$(1-\epsilon)^3\epsilon\sigma T^4$

$\epsilon^2(1-\epsilon^4)\sigma T^4$ $(1-\epsilon)^4\epsilon\sigma T^4$

etc.

So total flux of $478°$ radiation = $\epsilon^2 \sigma T^4 \left[1 + (1-\epsilon)^2 + (1-\epsilon)^4 + (1-\epsilon)^6 \dots \right]$

if $x = (1-\epsilon)^2$ the brackets equal $1 + x(1+ x(1+x(1+x)))$ etc   for $\epsilon = 0.16$, $[\ ] = 2.40$

for $\epsilon = 0.13$, $[\ ] = 3.11$

Reverse flux of $293°K$ radiation is same with sign reversal and ϵ_{293} used.

Net Flow is $H = \sigma \left(\epsilon_{478}^2 [\ ]_{478} (478)^4 - \epsilon_{293}^2 [\ ]_{293} (293)^4 \right) = 1.61 \times 10^5 \, \text{erg cm}^{-2} \, \text{s}^{-1}$

Temperature rise is $\dfrac{1.61 \times 10^5 \, \text{erg cm}^{-2} \, \text{s}^{-1}}{9.45 \times 10^6 \, \text{erg g}^{-1} \, ^\circ\text{C}^{-1} \quad 0.85 \, \text{g cm}^{-2}} = 0.020 \, ^\circ\text{C} \, \text{s}^{-1}$

Suppose we have 400 sec for expansion to occur, $\Delta T = 8 \, ^\circ\text{C}$
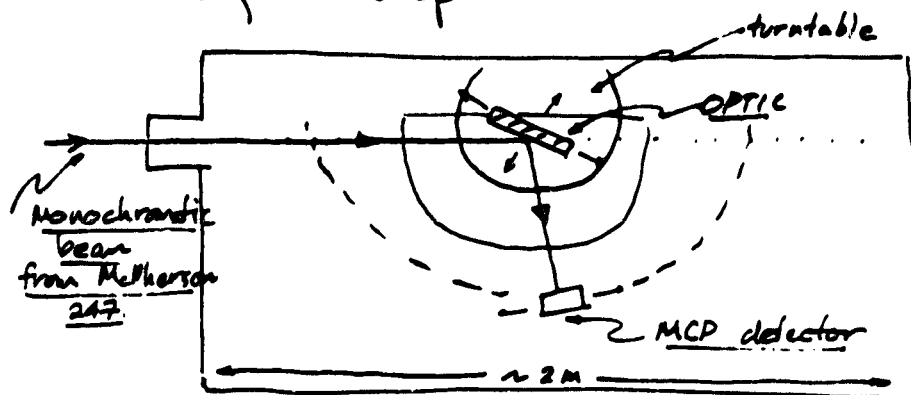which will cause 1800 mm path to lengthen by 0.37 mm

Image blur is then about 30μ if $f/10$.

The effect won't be so bad if outer skin cools.

The IMAPS cross disperser, echelle, and two small calibration mirrors were measured in the large reflectance facility at LASP between 3-7 and 3-15, 1984.

First, let me describe the laboratory setup:

TOP VIEW of VACUUM Chamber

The optics were illuminated by a beam of 'monochromatic' photons from a McPherson #247. The intensities of the reflected as well as the unreflected beams were measured with the same MCP detector, which is free to rotate about the 'center' of the optic, as shown above. The optics were mounted on a turntable which also provided linear motions in two directions in the plane of the sketch.

The cross disperser was measured first:
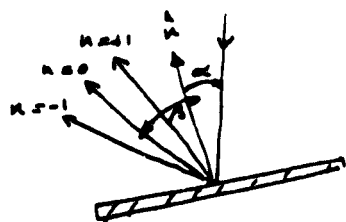
$\psi_{blaze} = 0.50°$, ruling density = 171.4 gr/mm.

I worked with an incidence angle of $\alpha \equiv 15°$, as measured from the normal to the plane of the grating.

The grating equation is

$$n\lambda = d (\sin\alpha + \sin\beta)$$

and with $\lambda = 1048\,\text{Å}$, we get

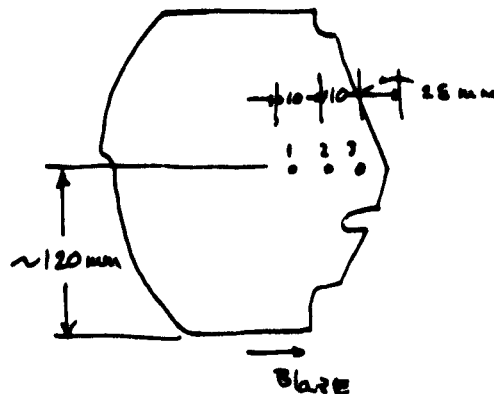| n	$\beta = \sin^{-1}\left(\frac{n\lambda}{d} - \sin\alpha\right)$
0	$-15°$
+1	$-13.9°$
+2	$-12.8°$
-1	$-16.07°$
-2	$-17.14°$

the blaze condition is satisfied when

$$|\alpha + \beta| = 2\psi$$

so obviously, $n = -1$ is the blazed order.

I measured 3 different spots on
the cross disperser :

The "reflectivity" R is calculated from

$$R = \frac{(Ncts - Backround)}{(N_{cts}(SOURCE) - Bckrnd)}$$

where N_{cts} is the # of cts/sec measured
in a particular order, $N_{cts}(SOURCE)$
is the # cts/sec of the unreflected beam,
and obviously Backround is the Backround
count rate due to electronics noise.

The results of the cross disperser are
as follows :

ORDER	R		
	# 1	# 2	# 3
+ 2		0.4 %	
+ 1	<0.1 %	0.7 %	0.2 %
0	2.4 %	3.0 %	1.3 %
− 1	(25.4%)	(28.7% ± 3%)	(23 ± 3.3%)
− 2	1.9 %	2.5 %	3.6 %

The error in R is computed in the usual way: if N is the # of cts, then $\delta N = \sqrt{N}$. One must take into account fluctuations in the beam intensity, background ct rate, and variation in MCP efficiency over the surface of the detector, which are $\sim \pm 1.5\%$.

Although I didn't do an extensive error analysis, to give you an idea of its magnitude, a typical unreflected beam intensity is ~ 2400 cts/sec, and all intensities were integrated over 60 seconds! The $\pm \sim 3\%$ in R, as shown, is typical.

I next measured the <u>two small</u> <u>test mirrors</u>. They are <u>labelled</u> # 1 and # 2:

1 : rather uniform reflectivity
<u>AVE. R $\sim 33\%$</u>

2 : varies alot across the surface (this one was mounted on the echelle)

<u>R $\sim 19\%$ to 29%</u>

Finally, the _echelle_ was measured:

$$\phi_{blaze} = 63.4549°$$

$$d = (79 \times 10^{-3})^{-1} \text{ Å}$$

This time, one spot on the echelle was measured, with 3 different angles of incidence.

As groove shadowing is extremely important here, the ideal situation is to have $\alpha = \beta$, as you have in the payload setup. Unfortunatly, our setup doesn't allow us to set $\alpha = \beta$, so I did 3 measurements that should show aproximatly what you'll get when $\alpha = \beta$.

The first measurement had $\alpha \simeq 78°$, so the blazed order was $n = 209$, with $\beta(209) \simeq 19°$. The detector lies a distance of 660 mm from the grating, which gives a physical separation of ~8mm between adjacent orders. Thus, the detector entrance aperature was set to ~10 mm to allow measurement of each order separatly. Unfortunatly, measurements of intensities between orders was therefore impossible.

In order for most of the light to be in one order (e.g. $n = 209$), the measurement involved 'tweaking' the grating and detector untill this condition is satisfied.

The results of this final measurement are as follows:

n	R	
208	9.0%	$\alpha - \beta \simeq 30°$
209	13.7%	
210	8.1%	

The next measurement was with $\alpha \simeq 71°$, $\beta_{(n=214)} \simeq 55°$. Thus, we have $\alpha - \beta \simeq 16°$:

n	R	
213	6.1%	$\alpha - \beta \simeq 16°$
214	18.0%	
215	5.9%	

The final measurement had $\alpha \simeq 69°$, and $\beta_{(215)} \simeq 58°$. Thus, $\alpha - \beta \simeq 11°$

n	R	
214	3.3%	$\alpha - \beta \simeq 11°$
215	20.3%	
216	6.5%	

The errors here are again on the order of a few percent for the blazed orders — the adjacent orders have a larger error due to the smaller count rate.

The effects of groove shadowing can be estimated as follows:
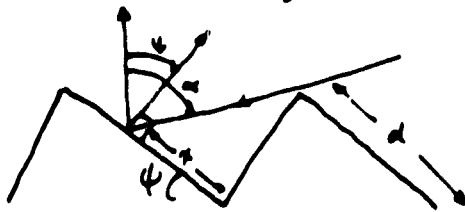
As can be seen from the drawing, the fraction of the groove face that is shadowed is x/d :

$$x/d = \tan(\alpha - \psi) \cdot \tan \psi$$

So with $\psi = 63.4°$,

$$\alpha_1 = 78° \qquad \Rightarrow \qquad 1 - x/d \simeq 48\%$$

$$\alpha_2 = 71° \qquad \rightarrow \qquad 1 - x/d \simeq 73.4\%$$

$$\alpha_3 = 69° \qquad \rightarrow \qquad 1 - x/d \simeq 80\%$$

The quantity $f = 1 - x/d$ represents the fraction of the groove face that is illuminated.

The ratio of the blazed order $(\equiv I_0)$ to an adjacent order $(\equiv I_\pm)$ can be predicted with a simple model :

$$\frac{I_\pm}{I_0} = \frac{I_0 \left(\frac{\sin \pi f}{\pi f}\right)^2}{I_0} = \left(\frac{\sin \pi f}{\pi f}\right)^2$$

which describes the result of shadowing on the blaze function

we can compare this model with the results
of the measurement:

f	$(\sin \pi f / \pi f)^2$	$(I_+ + I_-)/2 I_o$
(theoretical)		(MEASURED)
.48	43.8 %	62.4 %
.734	10.3 %	33.3 %
.80	5.5 %	24.1 %

As the measured ratio's are considerably
higher than that predicted with the
model, we can infere (if you believe
the model!) that more light is
going into the adjacent orders than
should be expected. This must be
due to imperfections in the grating.
(But remember that the errors in
the adjacent order efficiencies are higher
than the blazed order error.)

The difference between the
measured and theoitical values for
these line ratios is roughly constant
and gives ~ 20% of the blazed order
intensity falls into an adjacent order.
If we assume that this 20%
remains constant as $f \rightarrow 1$ (ie $\alpha = \beta = 4$)
then we can extrapolate the data
to get an idea of the $\alpha = \beta$ efficiency.

Let Δ be the fraction of light that is scattered into an adjacent order. The intensity of an adjacent order consists of a contribution from the $I_0(\sin \pi f/\pi f)^2$ part plus the scattered part: $\Delta \cdot I_0$. When $f \to 1$, the adjacent order intensity will be entirely due to ΔI_0.

Thus for a given f, we can add up all the intensities (e.g. $I_0 + I_+ + I_-$) and subtract off the part due to scattery. This number we call I' and we assume that when $f \to 1$, $I_0(f=1) = I'$.

For example, with $f = .48$

$$I' = I_0 + I_+ + I_- - 2(\Delta)I_0$$

$$= I_0(1 - 2(.20)) + I_+ + I_-$$

$$= 13.7\% (1 - .4) + 9.0\% + 8.1\%$$

$$\Rightarrow \underline{I' = 25.3\%}$$

the other f's give $\underline{\sim 23\%}$, and $\underline{\sim 22\%}$.

So with this <u>crude</u> model, one can guess that when $\alpha = \beta = 4$, you'll get $\underline{\sim 24\%}$ in the blazed order.

IUE echelle at 1216Å: 29%

Good luck with your instrument!

David Windt